Assessment of Snow Depth Retrievability from Passive Microwave Observations over Arctic Sea Ice: A Global Sensitivity Analysis

Ziyu Yan[1,2,3], Yufang Ye[1,2,3], Georg Heygster[4], Bin Cheng[5], Carolina Gabarró[6], Ferran Hernández-Macià[6], Xiao Cheng[1,2,3]

[1]School of Geospatial Engineering and Science, Sun Yat-sen University, Zhuhai, China
[2]Southern Marine Science and Engineering Guangdong Laboratory (Zhuhai), Zhuhai, China
[3]Key Laboratory of Comprehensive Observation of Polar Environment (Sun Yat-sen University), Ministry of Education, Zhuhai, China
[4]Institute of Environmental Physics, University of Bremen, Bremen, Germany
[5]Finnish Meteorological Institute, Helsinki, Finland
[6]Barcelona Polar Lab, Institute of Marine Sciences, Barcelona, Spain

Correspondence to: Yufang Ye (yeyf8@mail.sysu.edu.cn)

Abstract. The complexity of passive microwave (PM) retrieval of snow depth over Arctic sea ice stems from non-linear interactions between snow microstructure, wetness, and basal ice properties. These mechanisms remain insufficiently quantified, resulting in large uncertainties in PM-based snow products. We employ the snow microwave radiative transfer (SMRT) model together with a global sensitivity analysis, i.e. the Extended Fourier Amplitude Sensitivity Test, to decompose SMRT-simulated TB variance into contributions from individual parameters and their interactions. Averaging kernel analysis is then used to quantify snow depth retrievability across standard PM channels from 6 to 89 GHz under single- and multi-layer snowpack scenarios. 1) For single-layer dry snow, snow depth, density and grain radius are strongly coupled to each other, dominating the PM signals. When liquid water is present in the snow, the PM signals are primarily controlled by snow density and liquid water content. 2) In multi-layer dry snow, channels below 23 GHz are strongly influenced by the basal snow ice, while those above or equal to 23 GHz are dominated by depth hoar. At 6 GHz, retrievability is limited to dry snow with grain radius ≥ 0.5 mm and density ≤ 250 kg m^{-3}, expanding toward finer grains and higher densities with increasing frequency. Regarding gradient ratio (GR), GR(18/6) provides limited retrievability for grain radius < 0.5 mm, whereas GR(36/18) remains effective for grain radius ＞0.2 mm. Notably, incorporating 89 GHz in GR improves the retrievability for new snow. Furthermore, sea ice type exerts a significant constraint on GR retrievability of snow depth and becomes increasingly pronounced under fine-grained snow conditions.

1 Introduction

Snow is a key component of the Arctic climate system. Its high albedo and low thermal conductivity provide an insulation layer that significantly restricts heat transfer from the ocean through the sea ice (Landrum and Holland, 2022; Vérin et al.,

https://doi.org/10.5194/egusphere-2026-1680
Preprint. Discussion started: 28 May 2026

2022; Macfarlane et al., 2023). Snow depth can strongly influence the seasonal evolution of sea ice mass balance and the atmosphere–ocean-ice coupled system. Pan-Arctic observations of snow properties are therefore essential for advancing climate research and for improving the snow component in climate models (Zhou et al., 2021; Kacimi and Kwok, 2022).

Passive microwave remote sensing provides a unique capability for observing snow on sea ice under most weather and all-sky conditions. Multi-frequency radiometers, such as the Advanced Microwave Scanning Radiometer (AMSR) 2 and its successor AMSR3 measure the upwelling brightness temperature (TB) emitted from the Earth's surface. TB is influenced by various factors, most notably the frequency-dependent penetration depth, absorption, and scattering of radiation within the snowpack and the underlying sea ice (Markus and Cavalieri, 1998; Rostosky et al., 2018). Such physical mechanisms create fundamental ambiguities for snow depth retrieval. The TB response is not controlled by snow depth alone. It also depends on snow density, temperature, grain radius and bonding state (Picard et al., 2022a; Picard et al., 2022b; Soriot et al., 2022; Welch and Kelly, 2025). These parameters often co-vary in nature, and their combined effects on TBs can be strongly non-linear. As a result, many existing snow depth retrievals show pronounced seasonal and regional variability, and they can exhibit systematic biases when the actual snow microstructure deviates from the assumptions used in the algorithm (Yang et al., 2021; Gao et al., 2023; He et al., 2024). Because of the limited application ranges of existing snow depth retrieval algorithms, here we step back and suggest a more fundamental study on the snow and sea ice conditions under which retrieval of snow depth is possible and under which conditions it is not possible. In the remaining part of this introduction, we introduce the tools to be used for this purpose.

Radiative transfer modelling provides a physics-based analysis to quantify these effects and diagnose the retrievability of snow properties from passive microwave observations (Fuhrhop et al., 1998; Kang et al., 2019; Soriot et al., 2022; Wivell et al., 2023; Zhou et al., 2021). The Snow Microwave Radiative Transfer (SMRT) model can simulate AMSR2 multi-frequency and dual-polarisation TBs over parameterised Arctic snow and sea ice stratifications (Picard et al., 2018). To quantify how uncertainties in the snow properties propagate into TBs, it is necessary to evaluate model sensitivities across a plausible range of snow parameters. However, radiative transfer in snow is highly non-linear and state-dependent. As a result, local sensitivity tests can be misleading because parameter interactions may amplify or suppress sensitivities depending on the background conditions (Picard et al., 2013; Picard et al., 2018; Ottaviani et al., 2024). In this study, we aim to examine how the sensitivity of snow depth is modulated by snow microstructural properties, vertical stratification, snow wetness, and basal ice properties, while quantitatively assessing these effects within each AMSR2 observation channel. To this end, we adopt a global sensitivity analysis toolkit to quantitatively disentangle the contributions of individual parameters and their couplings to TBs. Here, "global" refers to the exploration of the full parameter space and their combined effects over the prescribed uncertainty ranges. Specifically, we apply the Extended Fourier Amplitude Sensitivity Test (EFAST) to decompose the variance of SMRT-simulated TB into contributions from individual parameters and from their couplings (Saltelli et al., 1999). This approach provides a unique quantitative ranking of parameter importance across prescribed ranges and makes it possible to identify regimes in which coupling effects dominate the TB variability (Marino et al., 2008). We are not aware of similar work done before.

Sensitivity ranking of a single parameter alone does not adequately answer the retrieval question. A parameter can be sensitive in a dimensionless variance decomposition sense while still being poorly retrievable because the effect of this single parameter on TB is degenerate with other parameters, masked by measurement noise or dominated by prior constraints (Rodgers, 2000; Tarantola, 2005). The quantitative assessment of the impact of multiple parameters on snow depth retrievability remains a knowledge gap, in particular the non-linear coupling of snow microstructure, liquid water content, and sea ice type. Quantitative benchmarks are needed to define, for example, the precise envelope of grain size and density within which 36 GHz observations provide sufficient information for a robust snow depth retrieval. Therefore, we complement the sensitivity analysis with the concept of retrievable range: the subset of the multidimensional parameter space in which the observations provide sufficient independent information to retrieve a target parameter. We quantify this idea using the averaging kernel matrix from the optimal estimation theory (Rodgers, 2000), which links the retrievability to both the assumed observation error covariance and the prior parameter covariance. By evaluating the diagonal averaging kernel elements across the sampled parameter space, we map where a given parameter is observation-driven and thus practically retrievable. To perform these analyses, it is necessary to define realistic ranges for snow properties throughout the Arctic winter, as well as representative values for the underlying sea ice. Among the currently available datasets, MOSAiC provides the most comprehensive observational basis for this purpose, owing to its extensive snow and sea ice measurements collected during the 2019–2020 winter season (Nicolaus et al., 2022). We therefore use MOSAiC observations as the primary basis for constructing the snow and ice parameter constraints adopted in this study.

2 Method

2.1 Snow microwave radiative transfer model

The SMRT model (Picard et al., 2018) solves the radiative transfer equation for a stratified snowpack by integrating layer-specific electromagnetic properties with microstructure-dependent extinction. It simulates emission, absorption, and multiple scattering processes within the snow and ice layers for multiple frequencies. This forward modelling enables consistent simulation of how variations in snow parameters propagate into TB responses, providing an essential foundation for sensitivity and retrievability analyses.

In this study, three configurations, single-layer snow, multi-layer snow, and coupled snow and sea ice stratification are considered. Snow is further classified into dry and wet conditions. SMRT provides multiple built-in options for microstructure representation and electromagnetic modelling, and the selected combination determines the parameterisation of snow. In this study, the sticky hard spheres (SHS) microstructure model is combined with the improved Born approximation (IBA) scattering solver (Mätzler, 1998), which is implemented as a standard configuration in SMRT and has been commonly applied in Arctic snow studies (Löwe and Picard, 2015; Picard et al., 2018; Vargel et al., 2020). Under the selected SHS+IBA configuration, each snow layer in SMRT is characterised by a set of snow parameters, including layer thickness, density, temperature, effective grain radius, and stickiness. Grain radius is determined by the size and shape of individual scatterers, whereas snow density is determined by the ice volume fraction. Together, these two parameters dictate the number of grains per unit volume. Stickiness further describes the degree of inter-granular bonding, clustering and sintering. During snow metamorphism, grain growth typically occurs concurrently with densification (Colbeck, 1982). A notable example is the strong correlation between grain radius and density in wind slab, which often consists of small, fragmented grains that are densely packed (Domine et al., 2008). For wet snow simulations, liquid water content (LWC) is additionally prescribed for each layer. TBs are simulated using SMRT for the twelve AMSR2 channels, and all simulations are performed at a fixed incidence angle of 55° (see Sect. 3.2). For each channel, SMRT computes the upwelling TB at the snow–air interface.

2.2 Global sensitivity analysis

We apply EFAST (Saltelli et al., 1999) to decompose the variance of SMRT TBs and to rank the contributions from individual parameters as well as from their interactions. In the EFAST, each input parameter is assigned to a unique angular frequency, and the model response is evaluated along a one-dimensional sampling curve in the multidimensional parameter space. The resulting response is expanded into a Fourier series, such that variance contributions from each parameter are encoded in the amplitudes of the corresponding spectral components. Based on the Fourier coefficients, EFAST provides variance-based sensitivity indices, including the single sensitivity index (SSI) and the total sensitivity index (TSI), which account for the isolated contribution of a parameter and its contribution including interactions, respectively. Accordingly, global sensitivity analysis is implemented in two steps. Firstly, for the forward model ($y = f(x),\ x = (x_1, x_2, \cdots, x_n)$), the space of the input variables ($x_i(s)$) is sampled along a curve defined as

$$x_i(s) = \frac{1}{2} + \frac{1}{\pi}\arcsin[\sin(\omega_i s + \varphi_i)]\,, \tag{1}$$

where $i = 1,2,\cdots,N$, and φ_i is a uniformly distributed random phase shift within the range of $[0, 2\pi)$, s represents the sample order from 1 to the total number of samples N and ω_i is the Fourier frequency, which can be calculated based on the sample size and interference factor:

$$\omega_{max} = \frac{N-1}{2M}, \tag{2}$$

where the N is the sample size for each input parameter, M is the given interference factor, which is usually set to 4.

Secondly, we input the samples into the SMRT, which in turn outputs are expanded by the Fourier series:

$$y = f(s) = \sum_{j=-\infty}^{\infty}\{A_j\cos(js) + B_j\sin(js)\}, \tag{3}$$

where the Fourier coefficients A_j and B_j are defined as:

$$A_j = \frac{1}{2\pi}\int_{-\pi}^{\pi} f(s)\cos(js)\,ds, \tag{4}$$

$$B_j = \frac{1}{2\pi}\int_{-\pi}^{\pi} f(s)\sin(js)\,ds, \tag{5}$$

https://doi.org/10.5194/egusphere-2026-1680
Preprint. Discussion started: 28 May 2026

over the domain of integer frequencies $j \in Z = \{-\infty, \cdots, -1, 0, 1, \cdots, +\infty\}$. The total variance of the model output is obtained as:

$$\widehat{D} = \frac{1}{2\pi}\int_{-\pi}^{\pi} f^2(s)ds - \left[\frac{1}{2\pi}\int_{-\pi}^{\pi} f(s)ds\right]^2 \approx 2\sum_{j=1}^{+\infty}\left(A_j^2 + B_j^2\right). \tag{6}$$

The partial variance $\widehat{D}_i$ of the individual parameter x_i is estimated based on the Fourier coefficients A_j and B_j with respect to its specific Fourier frequency ω_i as

$$\widehat{D}_i = 2\sum_{j=1}^{+\infty}\left(A_{j\omega_i}^2 + B_{j\omega_i}^2\right). \tag{7}$$

So, we can calculate SSI and TSI:

$$SSI_i = \frac{\widehat{D}_i}{\widehat{D}}, \tag{8}$$

$$TSI_i = 1 - \frac{\widehat{D}_{-i}}{\widehat{D}}, \tag{9}$$

where $\widehat{D}_{-i}$ stands for the variance contribution from all Analysis of Variance terms that do not involve the ith parameter, defined as $\widehat{D}_{-i} = \sum \widehat{D_k}\ , k \neq i$. The SSI represents the direct contribution of the ith parameter, whereas TSI measures its total contribution, including both its direct effect and all interaction effects with other parameters. If TSI is higher than SSI, it indicates that the parameter exhibits coupling effects with other parameters. The value obtained by subtracting SSI from TSI represents the magnitude of this coupling effect.

2.3 Retrievability analysis

While EFAST ranks snow parameters using dimensionless sensitivity indices, it does not directly assess whether a parameter is retrievable under a given snowpack configuration. In a highly non-linear radiative transfer model, sensitivities are state-dependent because coupling effects between parameters can cause the value of one variable to alter the response to others. Consequently, the practical retrievability of snow parameters from TBs can vary markedly across different snow structures. To address this issue, we introduce the concept of retrievable range to describe the conditions under which a given parameter can be effectively retrieved from passive microwave observations. We define the retrievable range as the subset of the multi-dimensional parameter space in which a specific parameter can be retrieved with adequate information content from TBs.

A parameter is considered retrievable when the observation provides sufficient independent information to reduce its uncertainty beyond what is implied by measurement noise and intrinsic variability. This notion of retrievability depends on the sensitivity of TBs to the parameter across channels, the observational noise of TBs, and the prior variability of the parameter itself. Following the uncertainty propagation and information content theory, we quantify this process using the averaging kernel matrix, a standard diagnostic within optimal estimation theory (Rodgers, 2000):

$$A = (K^T S_e^{-1} K + S_a^{-1})^{-1} K^T S_e^{-1} K, \tag{10}$$

where K is the Jacobian matrix containing the partial derivatives of simulated TBs with respect to snow parameters, S_a is the prior covariance matrix, and S_e is the observation error covariance. The diagonal elements of A, expressed as A_{ii}, indicate the degree to which each parameter is constrained by observations rather than by the prescribed prior. In this sense, the A_{ii} quantify the fraction of the retrieved variability attributable to observation information for parameter i, with values approaching 1 indicating strong observation-driven and values near 0 indicating a prior dominated. Thus, the averaging kernel diagonal provides a physically meaningful criterion for establishing the retrievable parameter space. Because the averaging kernel is rarely strictly binary, a practical threshold is required to classify whether a parameter is observational retrievable. Following the common practice in atmospheric and cryosphere studies (Hou et al., 2018; Stöffelmair et al., 2025), we adopt:

$$A_{ii} > 0.5\,, \tag{11}$$

as an operational criterion, indicating that the retrieval of the parameter is predominantly driven by the observations rather than the prior, and therefore is retrievable with meaningful independent information content. Conversely, parameters with A_{ii} below this threshold are regarded as weakly constrained by observations and are therefore not effectively retrievable from observations alone. This analysis not only identifies which parameters are retrievable but also delineates the specific regions in the parameter space, i.e. physical regimes, in which the observations become informative (see Sect. 4). By mapping A_{ii} across the sampled multi-dimensional parameter space, this study defines the retrievable range for snow depth under varying snow and sea ice conditions.

In this study, we quantify the retrievable range for snow depth using single-channel TBs and gradient ratios (GRs). For the prior uncertainty of snow depth, S_a is specified using an Arctic-wide estimate of natural variability. Following Rückert et al., (2023), we adopted S_a ($\sigma_{snow\ depth}$) = 0.2m for the prior uncertainty for snow depth retrievability analysis. For single-channel TBs, the observation error covariance (S_e) is specified using the nominal AMSR2 radiometric noise, assumed to be 1 K uncertainty for each channel. For the GR-based retrievals, S_e is derived by propagating the TB measurement uncertainty through the GR formulation. For a GR defined from two TB channels, TB_1 and TB_2,

$$GR = \frac{TB_1 - TB_2}{TB_1 + TB_2}\,, \tag{12}$$

the uncertainty of GR is approximated by first-order error propagation,

$$\sigma_{GR}^2 \approx \sum_{i\le 2}\left(\frac{\partial GR}{\partial TB_i}\right)^2 \sigma_{TB_i}^2 + 2\sum_{i<j\le 2}\frac{\partial GR}{\partial TB_i}\frac{\partial GR}{\partial TB_j}Cov\left(TB_i, TB_j\right), \tag{13}$$

where σ_{TB_i} denote the radiometric noise (set to 1 K here), and $Cov(TB_i, TB_j)$ is the uncertainty covariance between the two channels. Assuming uncorrelated channel noise ($\mathrm{Cov}(TB_i, TB_j) = 0$) and equal variances ($\sigma_{TB_1} = \sigma_{TB_2} = 1\,K$), Eq. (13) reduces to

$$\sigma_{GR} = \frac{2\sigma_{TB_i}}{\left(TB_i + TB_j\right)^2}\sqrt{{TB_i}^2 + {TB_j}^2}\ (i < j \le 2). \tag{14}$$

This σ_{GR} will used as the observation error for the GR-based snow depth retrieval in the retrievability analysis.

3 Data

3.1 MOSAiC observations

The snow parameter configurations in this study are based on MOSAiC in-situ observations (Frickenhaus et al., 2022; Nicolaus et al., 2022). MOSAiC was a year-long drift expedition in the central Arctic Ocean from September 2019 to October 2020, with the icebreaker Polarstern serving as the central observational platform. The compiled MOSAiC snow pit database includes 576 snow pits and provides profiles of snow depth, density, temperature, snow water equivalent, salinity, and micro-computed tomography (micro-CT) samples, with measurements collected using a broad suite of instruments across the expedition (Macfarlane et al., 2021). In this study, we use in-situ measurements of snow depth, temperature profiles measured using a waterproof thermometer with a needle probe, density profiles measured using a fixed volume density cutter, specific surface area (SSA) derived from micro-CT analyses, and snow salinity profiles from snow pit samples measured in the laboratory.

Although this study primarily focuses on snow, the underlying sea ice also exerts a non-negligible influence on snow radiative transfer. We use the MOSAiC ice core datasets, providing co-located profiles of sea ice thickness, temperature, salinity, density and brine volume fraction (BVF) (Oggier et al., 2024; Oggier et al., 2025). Ice cores were classified as first-year ice (FYI) and multi-year ice (MYI) and sampled independently. During each coring event, ice temperature was measured using the thermometer inserted into pre-drilled holes. Ice salinity was measured from melted 5 cm core sections with a conductivity meter. Ice density was measured on a separate density core using the hydrostatic weighing method. Relative BVFs were derived from the measured salinity, temperature, and density following Cox and Weeks (1983) for cold ice, and Leppäranta and Manninen (1988) for ice warmer than -2℃.

3.2 Microwave radiometer configuration

AMSR2 is a spaceborne passive microwave radiometer onboard the Global Change Observation Mission satellite, providing continuous global observations since 2012. AMSR2 measures upwelling microwave TBs at six frequency bands centred at 6.9, 10.7, 18.7, 23.8, 36, and 89 GHz (henceforth denoted as 6, 10, 18, 23, 36 and 89 GHz for simplicity), operating at a conical incidence angle of approximately 55°. In this study, AMSR2 frequencies and polarisations are explicitly represented in the SMRT model simulations, forming the basis for the global sensitivity analysis in which channel-specific responses of TB to snow depth variability and parameter interactions are quantified.

3.3 Layered snow scenarios

We use the MOSAiC data together with existing Arctic snow literature (Fuhrhop et al., 1998) to define the snow stratification and to constrain physically plausible ranges for the key snow properties. We consider 1) single-layer snow and 2) multi-layer snow representations and perform the sensitivity analysis separately for each configuration. The multi-layer dry snow is subdivided into three characteristic layers: wind slab, depth hoar, and a basal snow ice layer (Fig. 1a). The wind slab typically forms through wind driven redistribution and compaction, resulting in relatively high density and small grain radius. Depth hoar develops under strong vertical temperature gradients via metamorphism, producing relatively low density and coarse-grained structure. The snow ice layer forms near the snow–ice interface through flooding followed by refreezing, therefore more saline than the overlying snow (Maksym and Jeffries, 2001; Sturm et al., 2002). For wet snow conditions (Fig. 1b), the stratification was simplified into a wet snow layer and a basal superimposed ice layer, with the latter representing refrozen meltwater from snow that accumulates and freezes in the snow-ice surface. Fig. 2 presents the vertical profiles of snow density, temperature, salinity and grain radius measured during MOSAiC, presented separately for the winter dry snow period (November 2019 to May 2020) and the summer wet snow period (June to September 2020). Coloured points represent individual snow pits profiles in each month, whereas the black curve provides the ensemble central tendency at each height, with horizontal bars indicating the corresponding standard deviations. Grain radius (r_{snow}, mm) is derived from measured SSA and converted to an equivalent grain radius using (Domine et al., 2008):

$$r_{snow} = \frac{3}{\rho_{\mathrm{ice}}\mathrm{SSA}}, \tag{15}$$

where ρ_{ice} denotes the density of pure ice (910 kg m^{-3}). This conversion provides an effective microstructural descriptor that is consistent with the SHS parameterisation.

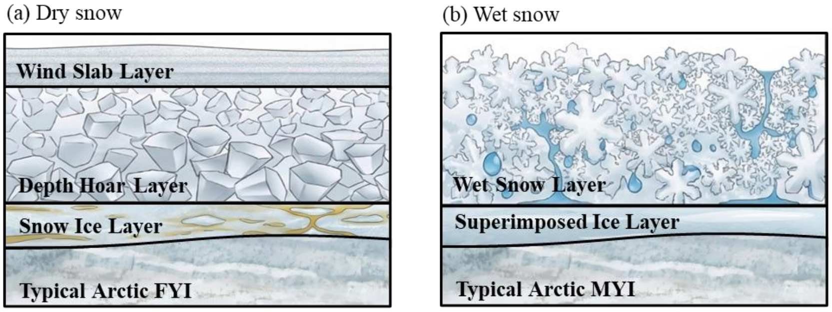

Figure 1: Conceptual diagrams of dry snow and wet snow layering over Arctic sea ice.

Based on the MOSAiC winter dry snow measurements, the layered snowpack is clearly expressed in the vertical increase of grain radius with depth (Fig. 2h). The upper snow is characterised by a small grain radius, consistent with a dense, fine-grained wind slab formed under wind compaction. With increasing snow depth, the grain radius progressively increases, ultimately transitioning to a coarse-grained layer that is characteristic of depth hoar. Snow salinity is often assumed to be negligible for Arctic snow, and the MOSAiC observations broadly support this assumption for snow layers above approximately 0.1 m, where salinity remains close to zero (Fig. 2d). However, MOSAiC also reveals a distinct regime in the near to basal snow (<10 cm), where salinity can increase sharply, reaching values as high as 10 (Fig. 2d). We conclude from this pronounced salinity enrichment that the snowpack cannot always be treated as a purely fresh medium near the snow–ice interface. Instead, it suggests the presence of an additional transitional layer between snow and sea ice, commonly referred to as snow ice in winter (Maksym and Jeffries, 2001), which inherits salinity from seawater and brine intrusion. Given that the SMRT model derives the BVF from salinity and temperature and subsequently uses it to simulate scattering, we directly parameterise snow ice using the BVF. The stickiness in the SHS is an effective parameter describing short-range spatial correlation among snow grains. In SMRT, it is used together with grain radius to control the simulated microwave scattering and emission. Since stickiness is not a strictly physical parameter itself, it is not discussed in further detail in this study. The physically plausible ranges of the corresponding snow layer parameters are presented in Tabs. 1 and 2.

For wet snow conditions, the presence of liquid water markedly alters both the microstructure and the thermodynamic properties of the snowpack. Once melt begins, liquid water increases inter-grain bonding and promotes rapid grain coarsening, while percolation and refreezing processes redistribute mass vertically and tend to homogenize the snowpack (Colbeck, 1974; Wever et al., 2014; Vuyovich et al., 2017). We represent wet snow in our simulations using a single snow layer, characterised by depth, density, LWC, grain radius and stickiness. Based on the MOSAiC measurements, wet snow temperatures remain close to the melting point (273.15 K) with only a small standard deviation throughout the melt season (Fig. 2g). Therefore, in the sensitivity analysis, the wet snow temperature was treated as a fixed parameter and set to 273.15 K. To ensure the validity of the Rayleigh scattering regime at 89 GHz, the effective grain radius was constrained to be less than 0.5 mm, following the established practices (Mätzler, 1998; Picard et al., 2018). This choice improves numerical stability and maintains physical consistency of the IBA-based scattering calculations in our simulation. In addition to wet snow melting, there often exists a superimposed ice layer at the snow–ice interface. Superimposed ice develops when meltwater generated within the snowpack percolates downward and refreezes upon reaching a colder underlying ice surface (Nicolaus et al., 2003; Granskog et al., 2006). Repeated melt–freeze cycles and sustained percolation can thicken this layer, which effectively modifies the lower boundary condition of the snowpack by increasing reflectivity and reducing permeability (Arndt et al., 2021; Wever et al., 2016). Tab. 3 presents the physically plausible ranges of the corresponding wet snow parameters.

Table 1 Single layer snow parameter ranges for global sensitivity analysis (Radius: snow grain radius)

Parameters	**Depth**	**Density**	**Temperature**	**Radius**	**Stickiness**	**Liquid water content**
Unit	m	kg m^{-3}	K	mm	-	%
Dry snow	[0, 0.6]	[150, 500]	[240, 270]	[0.1, 0.4]	[0.1, 0.3]	0
Wet snow	[0, 0.5]	[150,500]	273.15	[0.1, 0.5]	[0.1, 0.2]	[0, 10]

Table 2 Multi-layer dry snow parameter ranges for global sensitivity analysis (BVF: Brine volume fraction, Radius: snow grain radius)

Parameters	Depth	Density	Temperature	Radius	Stickiness	BVF
Unit	m	kg m^{-3}	K	mm	-	%
Wind Slab	[0, 0.2]	[200, 500]	[235, 265]	[0.05, 0.2]	[0.1, 0.2]	-
Depth Hoar	[0, 0.3]	[150, 500]	[245, 265]	[0.2, 0.5]	[0.1, 0.3]	-
Snow ice	[0, 0.1]	[600, 900]	[255, 270]	1	-	[0, 10]

Table 3 Multi-layer wet snow parameter ranges for global sensitivity analysis (Sup. ice: Superimposed ice)

Parameters	Depth	Density	Temperature	Radius	Stickiness	Liquid water content
Unit	m	kg m^{-3}	K	mm	-	%
Wet snow	[0, 0.5]	[150, 500]	273.15	[0.1, 0.5]	[0.1, 0.2]	[0, 10]
Sup. ice	[0, 0.1]	[600, 900]	[255,270]	0.1	0.3	-

3.4 Basal ice scenarios

In the snow sensitivity analysis, the basal sea ice layer needs to be specified with special care because it provides the lower boundary condition for radiative transfer through the snowpack. Arctic sea ice is commonly categorised into FYI and MYI, which differ primarily in their salinity and BVF. FYI typically retains higher salinity and larger BVF, whereas MYI is generally desalinated through brine drainage and melt processes, resulting in lower BVF (Cox and Weeks, 1974; Notz and Worster, 2009). For winter dry snow analysis, the underlying basal sea ice was assumed to be FYI, whereas for summer wet snow analysis it was assumed to be MYI. In addition, for winter dry snow, differences in microwave emission between FYI and MYI can bias snow depth retrievals, particularly for GR algorithms (Markus and Cavalieri, 1998; Rostosky et al., 2018). We therefore used the MYI fraction (MYIF), defined as the areal proportion of MYI over sea ice within the sensor footprint, to quantify and evaluate the potential impact of ice type variability on the snow depth retrieval. Guided by MOSAiC observations and accounting for the microwave penetration depth (<0.5m in sea ice at the lowest frequency), we represent the basal sea ice medium using a two-layer structure. The upper ice layer extends from the ice surface to 0.5 m depth, while the lower layer represents the ice below 0.5 m. In SMRT, the primary distinction between FYI and MYI is represented through the dominant scattering inclusions. For FYI, scattering is mainly associated with brine inclusions, whereas for MYI it is primarily governed by air bubbles, and MYI density is computed from the porosity in SMRT. Based on the contrasting physical characteristics of these scatterers, we prescribe scattering properties in the SMRT simulation (Shokr and Sinha, 1994; Tonboe, 2010; Picard et al., 2018). Each layer is parameterized by thickness, temperature, and either density/BVF (FYI) or porosity (MYI), as summarized in Tab 4. The ice temperature is assumed to be constant in both FYI and MYI at 265 K.

https://doi.org/10.5194/egusphere-2026-1680
Preprint. Discussion started: 28 May 2026

Table 4 Multi-layer sea ice parameters (BVF: Brine volume fraction, Radius: scatterer radius)

Parameters		Thickness	Density	Temperature	Radius	BVF	Porosity
Unit		m	kg m^{-3}	K	mm	%	%
FYI	Layer 1	0.5	910	265	0.1	5	-
	Layer 2	1.0	910	265	0.1	5	-
MYI	Layer 1	0.5	-	265	1.0	-	5
	Layer 2	1.5	-	265	1.0	-	5

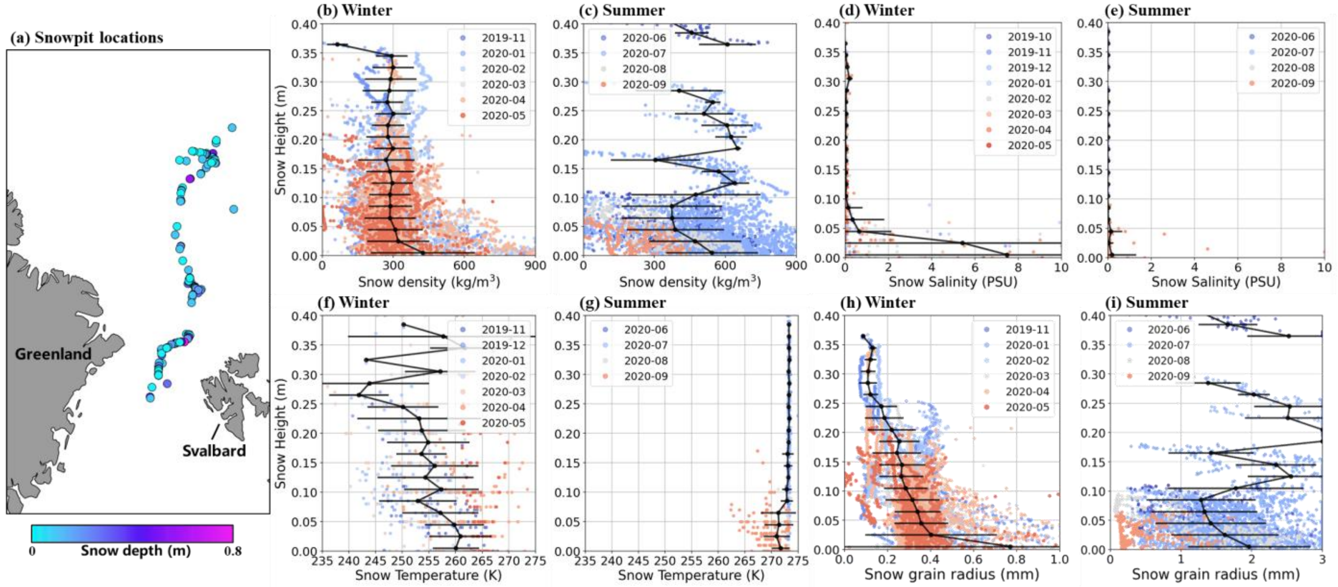

Figure 2: Stratified measurements of snow properties during the winter and summer months of the MOSAiC expedition. (a) locations of snowpit and snow depth, (b-c) snow density; (d-e) Snow salinity; (f-g): Snow temperature: (h-i): Snow grain radius. Colour points indicate measurements for each month, and black lines represent the ensemble central tendency of the corresponding profiles. The horizontal bars are the standard deviation at various depths.

4 Results

4.1 Global sensitivity analysis

4.1.1 Single-layer snow

Fig. 3 presents the EFAST sensitivity indices of single-layer snow for all AMSR2 channels under dry snow and wet snow conditions. Each vertical bar corresponds to one AMSR2 channel, and the different colours represent the sensitivity contribution from snow depth, density, grain radius, stickiness, temperature (only in dry snow) and LWC (only in wet snow), respectively. The solid segments show the single sensitivity index of each parameter, representing the fraction of TB variance

https://doi.org/10.5194/egusphere-2026-1680
Preprint. Discussion started: 28 May 2026

that can be explained by this parameter alone. The dotted extension of each solid segment represents the additional sensitivity captured by the total sensitivity, which includes not only the parameter's single effect but also all coupling effects between this parameter and the others. In other words, the dotted portion explicitly shows how much extra variance is explained when the coupling effects between this parameter and other parameters are included. It is important to note that these EFAST indices are relative measures defined within the chosen snow parameter set. Moreover, the information that each channel carries about the snowpack is not the same, because the penetration depth of the microwave signal and its physical interaction with the snow/ice pack vary with frequency. Consequently, a parameter may appear highly sensitive in one channel while that channel still does not contain sufficient independent information to robustly retrieve it. As an example, at low frequencies (6 GHz and 10 GHz), the information content of TBs about the snowpack is intrinsically weak, with most of the signal still originating from the underlying sea ice (Burgard et al., 2020). At these frequencies, snow density emerges as the dominant parameter, as its sensitivity indices are much larger than those of other snow parameters. However, changes in density lead to only modest variations in TBs (see Sect. 4.2).

Under dry snow conditions in winter (Fig. 3a), snow density is the dominant control on simulated TB between 6 and 18 GHz, with negligible coupling effects from other parameters except at 18 GHz. With increasing frequency, the sensitivity to density gradually decreases, becoming more evenly distributed among various snow parameters. Conversely, grain radius exerts a dominant control on simulated TB at high-frequency channels, particularly at 36 and 89 GHz. At frequencies above 18 GHz, the parameters governing snow microstructure, i.e. density, grain radius and stickiness, are subject to strong coupling effects. While their SSIs are modest, the corresponding TSIs are considerably larger. Consequently, neglecting the variability in snow density and grain radius can introduce significant biases in the snow depth retrieval. While several algorithms explicitly incorporate snow density in the retrieval of snow depth, they often rely on prescribed or climatological values (He et al., 2024). As a result, the temporal evolution of snow microstructure and its coupled effects on microwave scattering are generally not fully represented. Retrieval errors may arise when the true microstructural state of the snowpack deviates from these assumptions. Nevertheless, the parameter ranges adopted in this study are designed to encompass a broad variability of typical Arctic snow and sea ice conditions. While potential extreme outliers are not explicitly considered, they are unlikely to constrain the general findings of this analysis.

(a) Snow in winter: dry snow

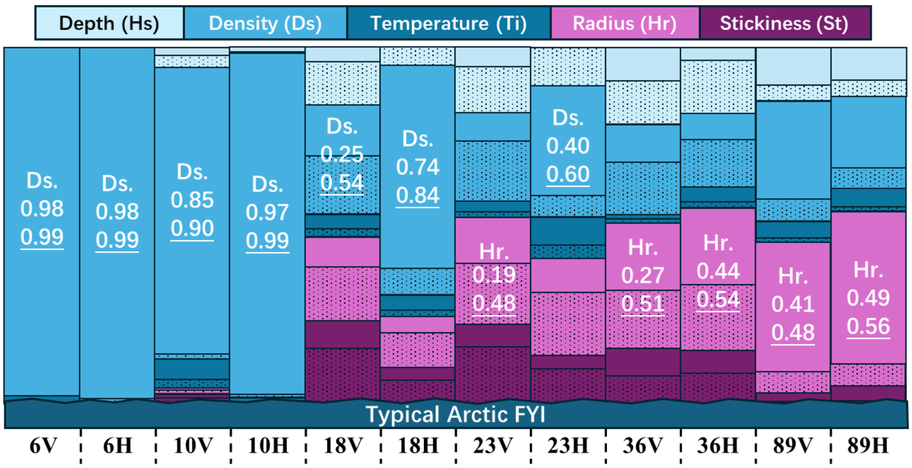

(b) Snow in summer: wet snow

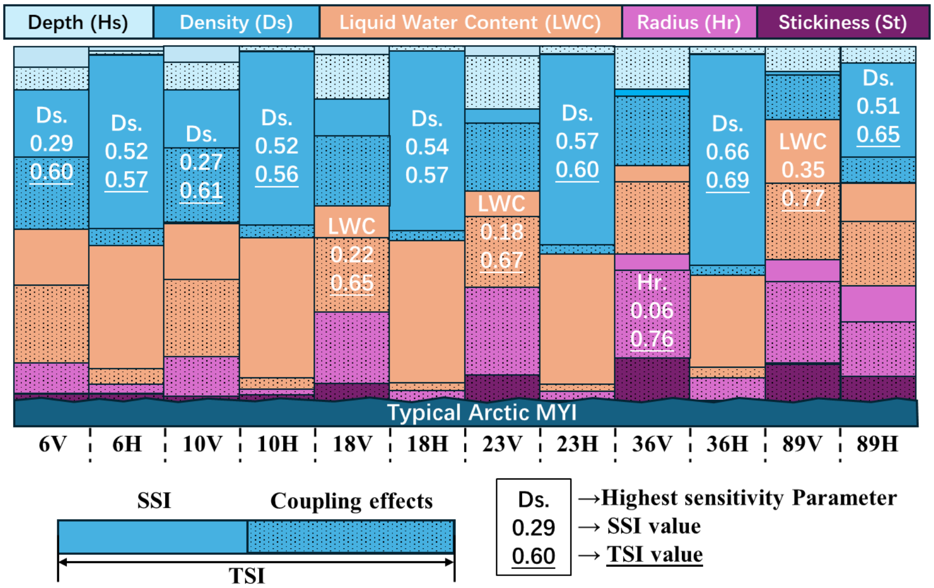

Figure 3: EFAST sensitivity result of single-layer Arctic snow parameters for the AMSR2 channels under dry snow (a) and wet snow (b) conditions. Solid segments indicate the SSI of each parameter, while dotted extensions show the coupling effects captured by the TSI. For each channel (column), the strongest single sensitivity and the total sensitivity are also given numerically.

4.1.2 Multi-layer dry snow

The multi-layer dry snow is idealized as an upper wind slab layer, an underlying depth hoar layer, and a basal snow ice layer. Fig. 4 presents the EFAST results for the multi-layer dry snow. Again, for each channel, the solid segments indicate the TSI, and the dotted segments represent the portion of coupling effects.

Between 6 and 18 GHz V-pol channels, the signal is almost entirely dominated by the snow ice layer, with snow ice temperature and BVF being the most sensitive parameters. In contrast, the dominant parameter shifts at Horizontal polarisation

(H-pol) channels, and the TB variance is controlled mainly by the density of the depth hoar, suggesting that H-pol at low frequency is comparatively less responsive to snow ice variability and more influenced by overlying snowpack structure. The 23 GHz channel sensitivities are broadly consistent with the 18 GHz behaviours in terms of polarisation contrast. However, the dominance of snow ice in 23 GHz V-pol weakens, and the sensitivity originating from wind slab and depth hoar increases. We also find that coupling effects are substantially stronger in the V-pol channels than in the H-pol channels, consistent with our single-layer sensitivity analysis (Fig. 3). At 23 GHz, coupling effects are no longer restricted to the snow ice layer. Depth and density of the depth hoar exhibit pronounced coupling effects with parameters in the snow ice layer, indicating both intra-layer and inter-layer dependencies. This result implies that retrievals of bulk snow properties such as snow depth and density from the 23 GHz V-pol channel are likely to be strongly influenced by the presence of snow ice. At 89 GHz, both the depth, density and grain radius of wind slab and depth hoar layers exhibit pronounced sensitivities. The radius in the depth hoar layer exerts strong control on volume scattering and thus on the 89 GHz signal.

Snow ice, depth hoar, and wind slab exhibit distinct sensitivity patterns across frequencies and polarizations. This suggests that multi-frequency passive microwave observations could be used to retrieve not only bulk snow properties but also the internal snow layering structure. For example, the 18 and 23 GHz V-pol channels can provide valuable information on the presence of snow ice. Given the widespread occurrence of snow ice over the Arctic sea ice (Merkouriadi et al., 2020; Merkouriadi et al., 2017) and its influence on the thermal insulation and seasonal evolution of sea ice mass balance, the ability to identify snow ice from these channels would be of considerable practical value. By contrast, 36 GHz stands out as an excellent frequency for observing the depth hoar layer, consistent with the fact that depth hoar is a dominant component of dry winter snowpack and that many existing snow depth retrieval algorithms are built upon the 36 GHz observations. However, the relatively low sensitivity of 36 GHz to the wind slab implies that the retrieval relying primarily on 36 GHz, even when combined with lower-frequency channels, may underestimate total snow depth in situations when a thick layer of wind slab is present, because the contribution of wind slab is effectively underrepresented in the microwave radiometric signal. In contrast, higher-frequency channels (e.g., 89 GHz) or spectral gradients such as GR(89/36) exhibit enhanced sensitivity to wind slab microstructure and layer thickness, as demonstrated in our sensitivity analysis (see the supplementary materials). Therefore, incorporating high-frequency information may help mitigate the underestimation biases and improve the detectability of wind slab, although the retrieval remains constrained by the properties of the underlying depth hoar.

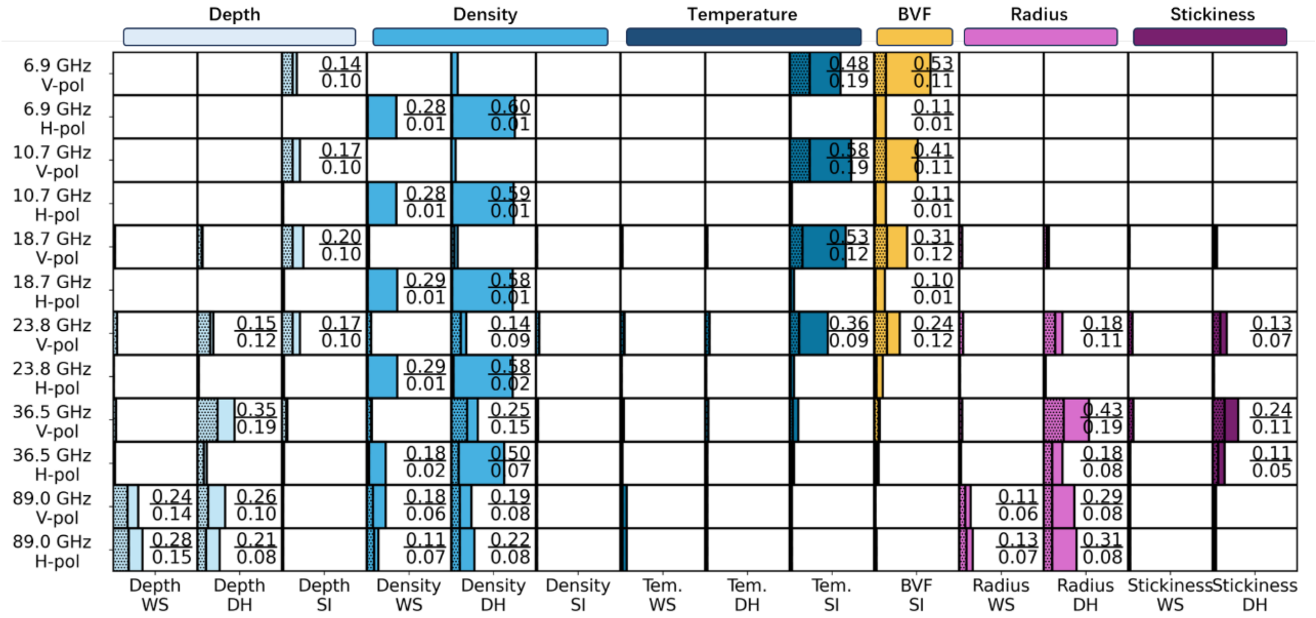

Figure 4: Multi-layer dry snow global sensitivity analysis result. Within each cell, solid segments indicate the TSI of each parameter, while dotted extensions show the portion of coupling effects. The upper underlined number denotes the total sensitivity index, and the number below denotes the coupling effects index. (WS: wind slab layer, DH: depth hoar layer, SI: snow ice layer.)

4.1.3 Multi-layer wet snow

Compared to dry snow, wet snow contains a non-negligible fraction of liquid water within the pore space. As shown in Fig. 5, the sensitivity results for wet snow differ markedly from those of dry snow. Between 6 and 18 GHz H-pol channels, the SSI and TSI exhibit a consistent pattern. Snow density and LWC in the wet snow layer account for nearly all the sensitivity, while other parameters yield TSI near zero. The 89 GHz H-pol channel behaves differently. While snow density and LWC remain the predominant sensitive parameters, superimposed ice properties (depth and density), as well as snow depth and radius, acquire non-negligible TSI. The corresponding coupling indices at 89 GHz are significantly larger than those at 18 - 36 GHz, although they remain lower in H-pol than in V-pol. This shift indicates that at 89 GHz H-pol, the emission is no longer governed solely by the bulk permittivity of a homogeneous wet layer. When the wet snow layer is of finite depth, reflections from the underlying superimposed ice and residual microstructural scattering also contribute to the signal. In this regime, snow density and LWC modulate the radiometric response not only through their effect on the effective permittivity but also through their influence on layer contrasts and shallow-volume scattering.

Across the 6 - 36 GHz, only snow depth, snow density and LWC exhibit some SSI, while other parameters, most notably snow grain radius and superimposed ice properties, have small direct effects. However, once coupling effects are considered, a different picture emerges. The coupling effects bring snow grain radius and superimposed ice depth to the foreground, leading to high TSIs even though their SSI are negligible. Moreover, the strength of coupling effects increases systematically with frequency. The strongest interactions involve snow and superimposed ice depth, snow density, grain radius and LWC.

Physically, LWC strongly influences the penetration depth of the wet snow layer and therefore modulates the degree to which the deeper layers are coupled to the observed radiation. At higher frequencies, the wet layer becomes increasingly absorbing, and residual microstructural scattering may contribute when the wet layer is not fully opaque. These processes jointly produce a more non-linear sensitivity of the TBs to combined variations in layer depth and LWC, effectively enhancing parameter coupling in the microwave radiometric response.

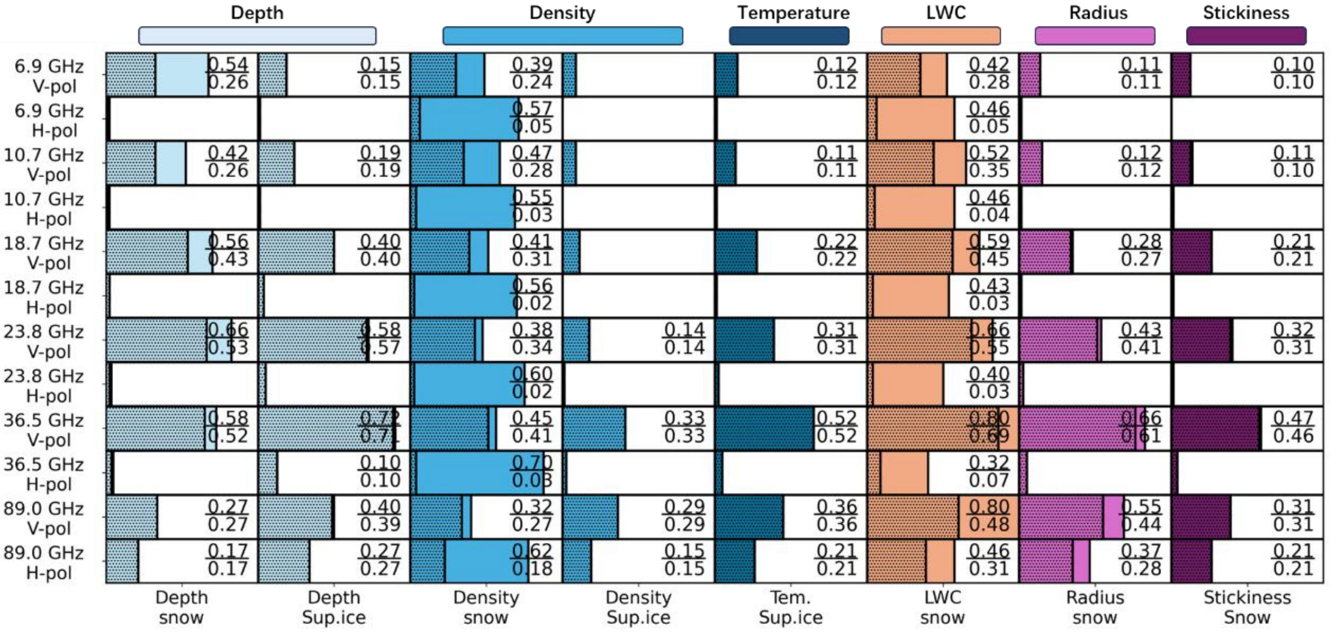

Figure 5: Multi-layer wet snow global sensitivity analysis. Within each cell, solid segments indicate the TSI of each parameter, while dotted extensions show the portion of coupling effects. The upper underlined number denotes the total sensitivity index, and the number below denotes the coupling effects index. (Sup. ice: superimposed ice)

4.2 Retrievable range of snow depth

Global sensitivity analysis offers a framework for identifying the snow parameters that most strongly influence TB and characterising how their interactions shape that influence. However, a critical remaining question is whether parameters exhibiting high sensitivity in specific channels can be retrieved robustly. Equally important is to quantify how parameter coupling impacts retrieval performance. This section builds on uncertainty propagation theory and introduces a new metric, the retrievable range, to define the parameter space where a given quantity can be reliably retrieved under varying background conditions.

In recent years, a wide range of snow depth retrieval algorithms have been developed using different passive microwave channels and modelling assumptions (Markus and Cavalieri, 1998; Rostosky et al., 2018; He et al., 2024). However, retrieval ambiguity remains because other factors, like snow grain radius and the radiometric contribution from the underlying sea ice, also exert strong impacts on TBs. In this section, we focus on three snow physical parameters that exhibit the strongest coupling effects in our sensitivity analysis (Fig. 3) — snow depth, density and grain radius, and evaluate the retrievable range of snow

https://doi.org/10.5194/egusphere-2026-1680
Preprint. Discussion started: 28 May 2026

depth based on single V-pol TBs and a suite of GRs. The evaluation is conducted across a range of snow microstructural states and underlying sea ice conditions.

4.2.1 Retrievable range with TBs

Fig.6 illustrates the corresponding retrievable range of snow depth diagnosed using the averaging kernel analysis. The columns correspond to different AMSR2 channels. The top row shows the TB response as a function of snow depth and density, with stacked layers representing different snow grain radius values. The second row adopts the same depth–density coordinate system and the same set of grain radius layers, but with colours depicting the diagonal averaging kernel element A_{ii} associated with snow depth. The bottom rows convert these averaging kernel diagnostics into a retrievable range for discrete grain radius values. The dark red regions indicate the retrievable range, defined as the projection onto the X–Y plane of the corresponding layers where the A_{ii} exceeds 0.5 (See Sect. 2.3).

The variation of TBs with snow parameters clearly increases with frequency (Fig. 6). At 6 and 10 GHz, the TB surfaces are nearly flat over a wide range of snow depth and density, and different grain radius layers are tightly clustered. Moving to 18, 23, and 36 GHz, the TB dependence on snow depth and density becomes progressively stronger, and the separation among grain radius layers increases. For frequencies up to 36 GHz the TB response shows no clear saturation within the tested snow depth range. In contrast, at 89 GHz the TB rapidly saturates and approaches an asymptote for sufficiently thick snow, indicating that the measured TB is dominated by the upper layer and further increases in snow depth produce only negligible changes in the signal.

The retrievable range of snow depth shows a clear frequency dependence, expanding toward smaller grain radius as the frequency increases. Between 6 and 18 GHz, snow depth retrievability remains limited and is primarily confined to cases with large grain radius. At those frequencies, only sufficiently large grains produce enough scattering contrast for snow depth to be independently retrieved. At 23 GHz, the retrievable range for snow depth emerges across all grain radius cases but remains strongly constrained by snow density. In particular, retrievability is limited to low density snow for fine grain, whereas such a combination of fine grains with low density is uncommon in natural snow. The retrievable range analysis indicates that channels from 6 to 36 GHz are generally unable to robustly retrieve snow depth under the high density and fine grain radius condition. Even at 36 GHz, when the grain radius = 0.1mm, the retrievable range may cover roughly snow density of 200 - 320 kg m^{-3}, which still falls short of the density levels frequently observed in fresh snow. Field observations suggest that fresh snow density commonly exceeds 300 kg m^{-3} and can approach 500 kg m^{-3} under wind packing (Domine et al., 2011). On the other hand, large grains typically emerge through strong metamorphism and are commonly associated with relatively low density (Domine et al., 2007; Schleef et al., 2014). Consequently, even though the 6 GHz retrievable range at 0.5 mm radius may only span a narrow density range, it can still contribute meaningful snow depth information for realistic metamorphosed and coarse-grained snowpack. 89 GHz V-pol is less constrained by snow density than other channels, especially when the grain radius is 0.1 mm, the retrievable range of snow depth covers the full density range. For fine-grained and high-density snow (e.g., wind slab layer), the 89 GHz V-pol TB is largely depth-dominated. However, 89 GHz is the only channel that saturates with snow depth. When the grain radius is 0.1 mm, the retrievable range of snow depth becomes saturated at around 0.7 m. As the grain radius increases, the retrievable range of snow depth progressively shrinks. The 89 GHz TBs are also susceptible to atmospheric effects (e.g., water vapour and cloud liquid water), which can introduce additional uncertainty into snow depth retrievals. Employing an atmospheric radiative transfer model for atmospheric correction is therefore an effective way to mitigate these impacts (Ye et al., 2025). In the Supplementary Materials, we correct AMSR2 TBs for atmospheric effects and find that the corrected 89 GHz channels are well suited for snow depth retrieval—particularly for fresh snow.

Between 6 and18 GHz, the TB sensitivity to grain radius is strongly density dependent. As snow density decreases, the TB contrast among different grain radius layers (First rows in Fig. 6) becomes more distinct, indicating that scattering differences induced by grain radius changes are more efficiently expressed in TB. This behaviour points to a strong coupling between grain radius and snow density at low frequencies. However, this coupling effect weakens markedly at 36 and 89 GHz. In particular, at 89 GHz the separation among different grain radius layers (Fig. 6f) is largely insensitive to changes in snow density, implying that the influence of grain radius on TB is both pronounced and effectively independent of density. For low frequency channels, the radiometric impact of grain radius becomes evident mainly under low density and thick snow conditions and remains strongly correlated with density. Consequently, retrievals rely on 6 - 23 GHz, can often achieve reasonable performance by accounting for snow density while neglecting grain radius, with only limited residual bias attributable to microstructure. In contrast, at 36 and 89 GHz the effect of grain radius is largely decoupled from density and remains significant across the explored density range. Under such usage, incorporating density alone does not resolve microstructural ambiguity, and neglecting grain radius can therefore introduce substantial biases in snow depth retrieval.

https://doi.org/10.5194/egusphere-2026-1680
Preprint. Discussion started: 28 May 2026

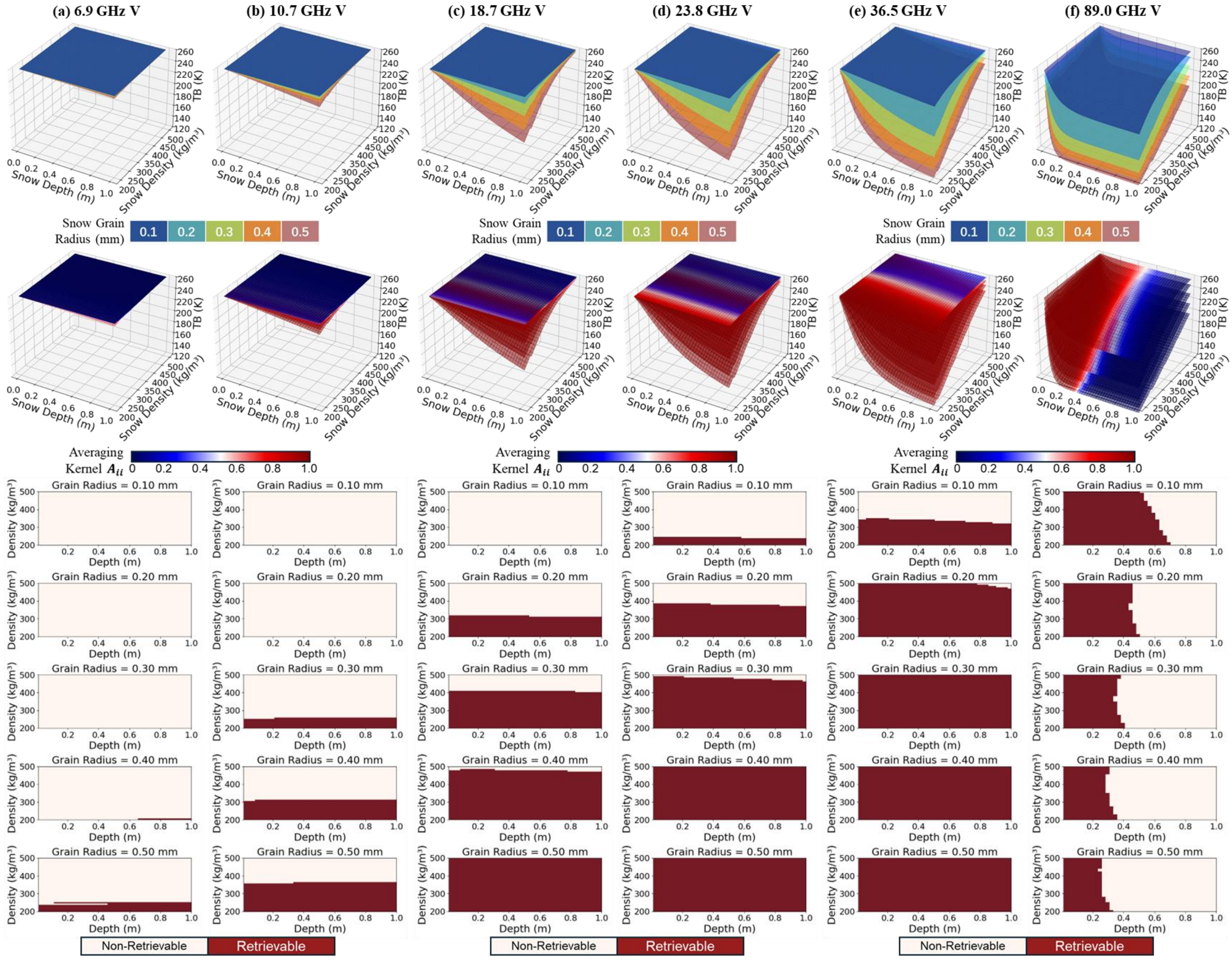

Figure 6: Retrievability of snow depth at 6 - 89 GHz V-pol channels. Top row: TB as a function of snow depth and density for different snow grain radius. Second row: corresponding diagonal averaging kernel element A_{ii} for snow depth. Bottom rows: retrievable ranges for discrete snow grain radius, defined as the projection onto the X–Y plane of the corresponding radius layers where the A_{ii} exceeds 0.5.

4.2.2 Retrievable range with GRs

Retrieving snow depth over sea ice surface from passive microwave observations is primarily based on GRs, most commonly the GR algorithms using 36 and 18 GHz (GR(36/18)) (Markus and Cavalieri, 1998) as well as 18 and 6 GHz (GR(18/6)) (Rostosky et al., 2018). As shown in Fig. 7, we evaluate the sensitivity of these two GRs to snow grain radius and density, and quantify the corresponding retrievable range for snow depth.

GR(36/18) is markedly more sensitive to fine-grained snow than GR(18/6). However, the GR(36/18) response tends to saturate near 0.5 m, implying a rapidly diminishing sensitivity and thus limited capability to discriminate thicker snow beyond

https://doi.org/10.5194/egusphere-2026-1680
Preprint. Discussion started: 28 May 2026

this range. In contrast, at a grain radius of 0.5 mm, the GR(18/6) retrievable snow depth range extends to 0 - 1 m, suggesting an advantage in coarser-grained snow. This aligns well with the fact that the GR(18/6) algorithm was originally developed using the Operation IceBridge observations, with the underlying relationship primarily constrained by the Arctic ground-truth data collected in March and April (Rostosky et al., 2018). During late winter to early spring, Arctic snow often undergoes pronounced metamorphism, with increasing grain radius and the development of a low-density, thick depth-hoar layer in many regions (Sturm and Benson, 1997). These conditions could enhance the influence of deeper snow layers on the lower frequency channels, making GR(18/6) comparatively more sensitive to snow depth than GR(36/18) under depth hoar dominated conditions.

GR(18/6) shows sensitivity to snow density and grain radius that is comparable to the behaviour observed for the 18 GHz V-pol channel. By contrast, GR(36/18) exhibits a markedly different sensitivity pattern to both snow density and grain radius relative to either the 36 GHz or 18 GHz channels. In particular, the difference in GR(36/18) between layers with grain radius of 0.1 mm and 0.3 mm is large, whereas the difference between 0.3 mm and 0.5 mm layers is minimal. This indicates a saturation of GR(36/18) with respect to grain radius. Furthermore, under low snow density conditions, GR(36/18) appears largely insensitive to further increases in grain radius. This implies that for snowpack characterised by relatively large grain sizes and low densities, where depth hoar is the dominant snow type, GR(36/18) is not strongly affected by variations in snow grain radius. This behaviour contrasts with that of GR(18/6), which exhibits a substantially higher sensitivity to grain radius than GR(36/18).

These results highlight the distinct application regimes of different GR algorithms and their varying susceptibility to interference from snow microstructure. Constrained by the penetration depth of the 36 GHz channel, GR(36/18) is only suitable for retrieving snow depth within approximately 0 - 0.5 m, as demonstrated in previous studies (Markus and Cavalieri, 1998). In contrast, GR(18/6) extends the snow depth retrievable range up to 1 m under large grain snow conditions.

In addition, we investigate four alternative GR combinations: GR(36/10), GR(36/6), GR(23/10), and GR(23/6). First, replacing the 18 GHz channel in GR(36/18) with 10 or 6 GHz exploits the deeper penetration and weaker scattering extinction at lower frequencies, which can delay saturation under thicker snow and thereby potentially expand the retrievable range of snow depth. Second, the use of the 23 GHz channel instead of 18 GHz in combination with lower frequency channels may be advantageous for snow characterised by intermediate grain radius. The retrievable ranges of snow depth using the four alternative GR combinations are shown in Fig. 8.

Overall, combining 36 GHz with lower frequencies expands the retrievable range relative to GR(36/18). Both GR(36/10) and GR(36/6) yield retrievable ranges encompassing snow depths of 0 - 0.6 m. This suggests that substituting 18 GHz with 10 or 6 GHz increases penetration contrast while retaining the scattering sensitivity of the high frequency. The difference between GR(36/6) and GR(36/10) is modest. Across the examined grain radius, their retrievable ranges are similar. This indicates that the dominant limitation is not the low frequency penetration, but rather the tendency of the 36 GHz–based GR to approach saturation as snow depth increases. Although the single-channel analysis shows that 36 GHz TBs remain sensitive for snow depth of 0 - 1 m (Fig. 6), saturation occurs when integrated into a GR. This is because the GR retrievability is governed by the

510 incremental depth information available after combining channels. As snow depth increases, slope of the 36 GHz TB relative to snow depth decreases. This has a strong impact on the 36 GHz-based GRs, causing the GR slope to collapse even when the 36 GHz TB is still slowly changing. Consequently, the remaining GR variations are readily masked by microphysical uncertainties and measurement noise, leading to apparent saturation in GR-based snow depth retrieval.

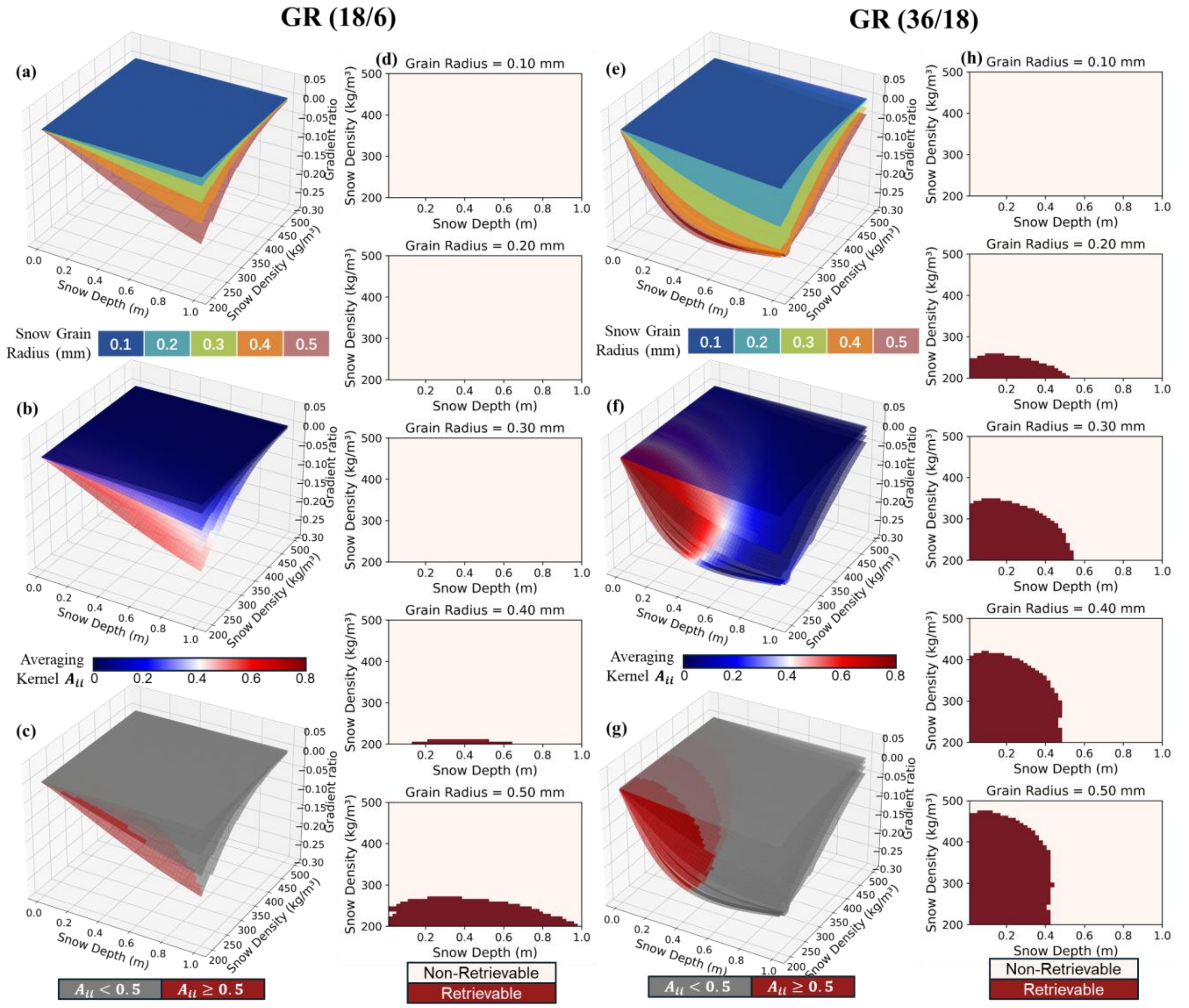

515 **Figure 7: Retrievability of snow depth with GR(18/6) (a-d) and GR(36/18) (e-h) on different snow density and grain radius (Snow temperature = 260 K, Stickiness = 0.1).**

For intermediate snow grain radius (0.3 - 0.5 mm), GR(23/6) exhibits a broader retrievable range for snow depth than GR(18/6). This enhanced sensitivity corresponds to a more extensive retrievable domain, with GR(23/6) supporting snow

https://doi.org/10.5194/egusphere-2026-1680
Preprint. Discussion started: 28 May 2026

depth retrievals up to approximately 1 m. Moreover, GR(23/6) provides an expanded retrievable range relative to GR(23/10). This contrasts with the 36 GHz scenarios, where the performance of GR(36/6) and GR(36/10) is nearly indistinguishable. Such discrepancies suggest that selection of the high frequency anchor in GRs fundamentally dictates the total information content available for snow depth retrieval.

When a high-frequency channel (e.g., 36 GHz) is used as the anchor, the retrievable snow depth range is limited. In contrast, this depth limitation is less severe for a 23 GHz anchor. In the coarse grain regime (e.g., grain radius of 0.3 - 0.5 mm), the 23 GHz response remains informative at greater snow depth, allowing GR(23/6) in particular to retain measurable sensitivity up to 1 m. The primary trade-off occurs for fine-grained snow, especially within the 0.1 - 0.3 mm radius range. In this regime, 23 GHz-based GRs lose sufficient sensitivity, resulting in a limited retrievable range. In early winter, newly formed snow is typically fine-grained. The strong high-frequency scattering contrast associated with the 36 GHz anchor is advantageous for achieving usable sensitivity in thin snowpack. Therefore, GR(36/10) or GR(36/6) is expected to be more suitable for early-winter conditions. As the season progresses toward late winter and spring, snow metamorphism increases the effective grain radius and stratigraphic complexity. Under such conditions, the 23 GHz anchor becomes more favorable. GR(23/10) and GR(23/6) can extend the retrievability into thick snow regime, which is not achievable with the 36 GHz anchor. Hence, for snow in late winter or spring, incorporating the 23 GHz channel in combination with lower frequencies may achieve robust snow depth retrieval. Furthermore, experiments that explicitly account for atmospheric effects indicate that despite 23 GHz being situated on the water vapor absorption line, GR(23/6) remains insensitive to atmospheric perturbations (See supplementary material).

4.2.3 Retrievable range over different ice types

Snow depth retrieval performance often exhibits a strong dependence on whether the snowpack overlies FYI or MYI. This relationship is critical because FYI and MYI differ significantly in their electromagnetic properties, which modulates the sensitivity of measured TB to snow parameters relative to the underlying ice substrate. We evaluate the sensitivities of various GRs commonly used for snow depth retrieval to both MYIF and snow grain radius and subsequently quantify the corresponding retrievable ranges. The specific microphysical parameter settings adopted for FYI and MYI are detailed in Sect. 3.4. For mixed ice type conditions, the total microwave emission is computed by linearly weighting the separate TB simulations for FYI and MYI based on the MYIF.

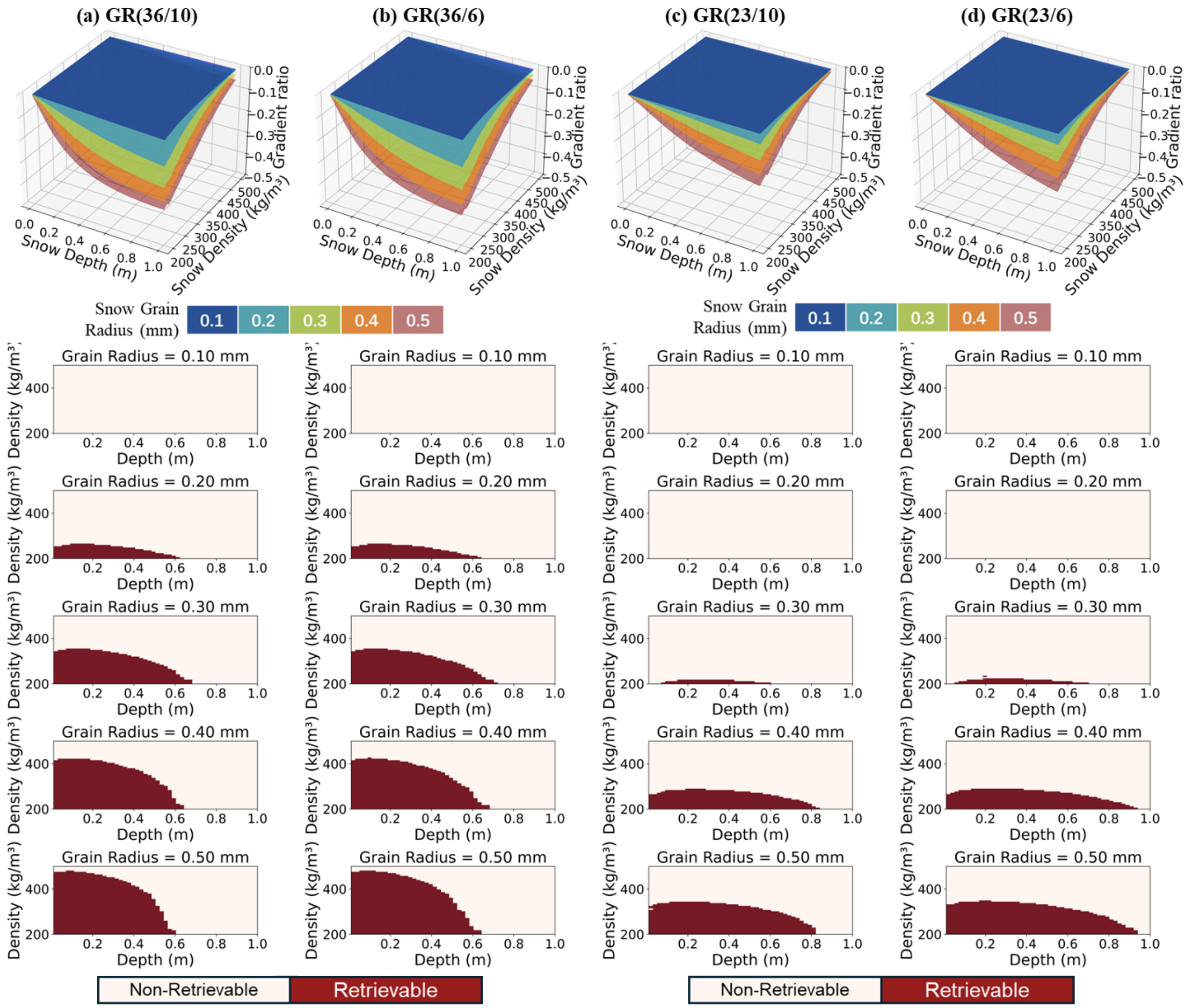

Figure 8: Retrievability of snow depth with GR(36/10), GR(36/6), GR(23/10) and GR(23/6) on different snow density and grain radius (Snow temperature = 260 K, Stickiness = 0.1).

Fig. 9 presents the joint sensitivity and the corresponding retrievable range of different GRs to snow depth under different MYIF. A consistent feature across GR(36/18) and GR(36/6) is that the retrievable range for snow depth decreases systematically with increasing MYIF. This degradation is most pronounced under fine-grained snow conditions, where the GR signal is already weak and therefore more vulnerable to confounding changes driven by the underlying ice state. For example, in GR(36/18) at radius = 0.3 mm, increasing MYIF from 0% to 100% reduces the snow depth retrievable range from approximately 0 - 0.5 m to 0 - 0.3 m. Replacing the 18 GHz with lower frequencies partially mitigates this limitation. At radius = 0.2 mm, GR(36/6) yields a modest expansion of retrievable snow depth relative to GR(36/18). More importantly, for coarse-grained snow, the use of 6 GHz enlarges the retrievable range of snow depth. This indicates that, over MYI surfaces, using a lower-frequency companion channel can partly compensate for the MYIF-induced loss of retrievable range observed in

https://doi.org/10.5194/egusphere-2026-1680
Preprint. Discussion started: 28 May 2026

GR(36/18). An additional notable behaviour emerges in GR(36/6): as MYIF increases, GR(36/6) becomes positive over parts of the parameter space in our simulation, indicating a reversal of the inter-frequency TB contrast. This implies that MYI can dominate the GR signal and outweigh the snow depth contribution. Such a regime is problematic for snow depth retrieval because GR is no longer primarily controlled by snow depth, when GR becomes strongly conditioned on ice type and other confounding factors.

Compared to GR(36/6), both GR(18/6) and GR(23/6) exhibit more positive values. The expanded positive GR domain indicates a strong susceptibility to the underlying ice state. For GR(18/6), the snow depth retrievable range exhibits a hump shaped pattern and reduced retrievability toward both shallow and deep extremes. In contrast, GR(23/6) substantially expands the retrievable range at high MYIF compared with GR(18/6). These results suggest that replacing 18 GHz with 23 GHz enhances the snow scattering contrast while preserving sufficient penetration depth to maintain snow depth sensitivity, thereby improving the response to snow depth when underlying ice properties strongly influence the radiometric signal.

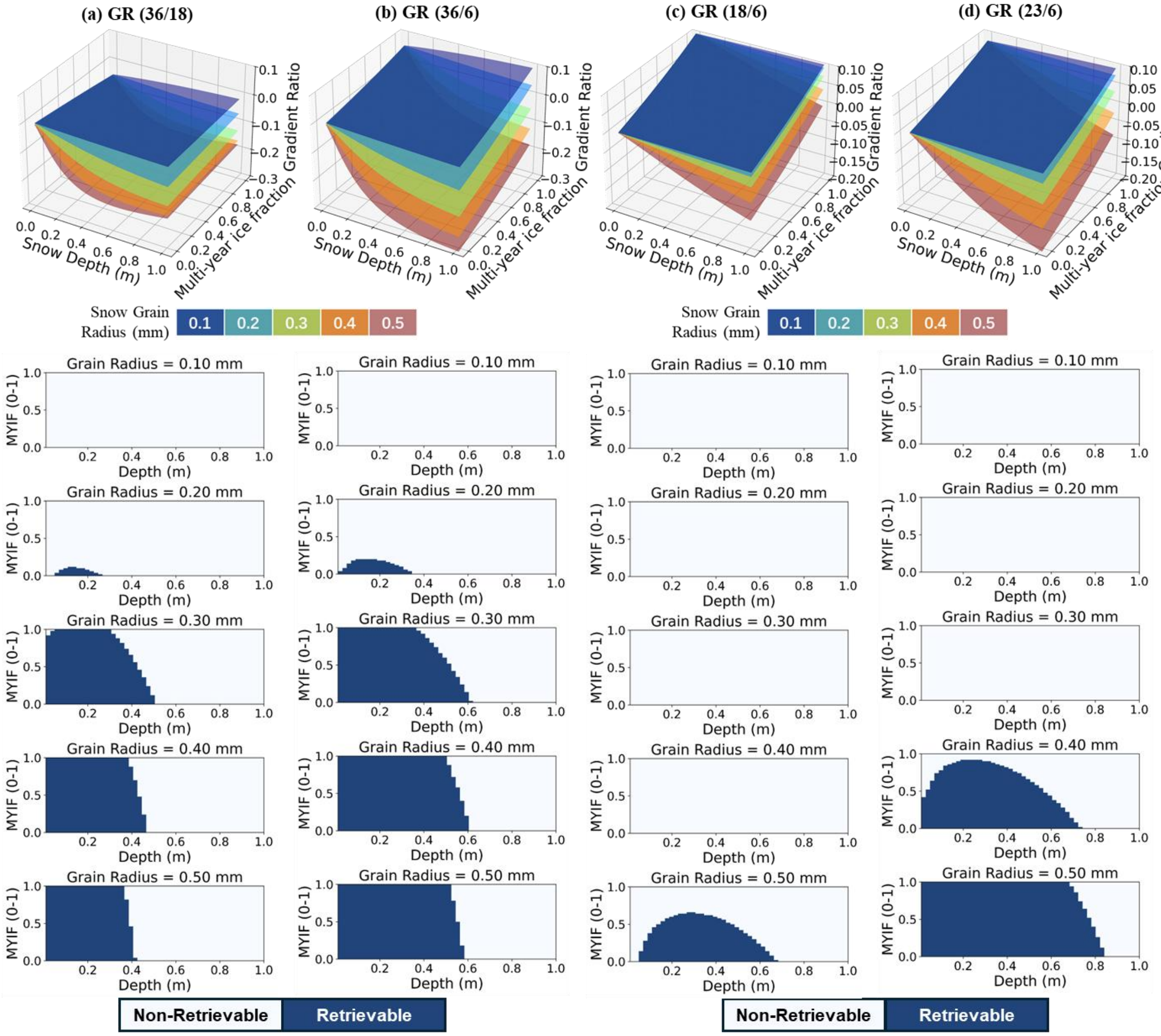

Figure 9: Retrievability of snow depth with GR(36/18), GR(36/6), GR(18/6) and GR(23/6) on different MYIF and grain radius. Top row: GR as a function of snow depth and MYIF for different snow grain radius (with fixed snow density of 260 kg m^{-3}). Second row: retrievable ranges for discrete snow grain radius, defined as the projection onto the Depth–MYIF plane of the corresponding radius layers where the A_{ii} exceeds 0.5.

5 Conclusions

By employing the EFAST global sensitivity analysis and the SMRT model, we quantitatively assessed the impacts of individual snow and ice physical parameters and their inter-parameter coupling on passive microwave observations. Our results demonstrate that the variability of TBs above 18 GHz is driven primarily by non-linear interactions among snow parameters rather than by isolated single-parameter effects. Based on the sensitivity analysis, we formulated the retrievable range of snow depth over sea ice under multi-dimensional regimes, providing a quantitative metric for assessing where passive microwave data offer effective information for snow depth retrieval.

For dry snow conditions, snow density and grain radius dominate the sensitivity at low-frequency and high-frequency channels, respectively. Snow depth begins to exhibit measurable sensitivity from 18 GHz onward; however, such sensitivity is heavily modulated by snow density and grain radius (Fig. 3). This indicates that snow depth sensitivity is not independent but varies substantially with changes in snow microstructure. Under wet snow conditions, the presence of liquid water fundamentally restructures the sensitivity ranking and the coupling effects. The TSI of LWC becomes comparable to or larger than that of snow density or grain radius. Furthermore, the enhanced absorption associated with liquid water strongly suppresses the sensitivity of snow depth and grain radius, particularly in horizontally polarized channels.

For multi-layer dry snow stratified into wind slab, depth hoar, and basal snow ice, the sensitivity patterns are polarization-dependent (Fig. 4). The H-pol channels are primarily sensitive to snow density, with generally weak inter-parameter coupling. In contrast, the V-pol channels exhibit strong layer-dependent sensitivity and pronounced coupling. Between 6 and 18 GHz V-pol, the TB variability is mainly controlled by the snow ice temperature and BVF. As the frequency increases, this snow ice dominance progressively weakens, while the contribution from the depth hoar layer strengthens, and inter-layer coupling between depth hoar and snow ice becomes increasingly significant. The 89 GHz TB is most sensitive to the wind slab layer, while retaining a non-negligible influence from the depth hoar. For the wet snow with basal superimposed ice, the TSI of the superimposed ice layer is almost entirely explained by coupling effects, with its SSI being close to zero. This implies that superimposed ice does not independently contaminate snow depth retrieval, and its detectability is conditional on the snow state.

Using the retrievable range analysis, we quantitatively assessed how the coupling among snow density, grain radius, and snow depth constrains practical retrievability of snow depth. Snow depth retrieval is jointly limited by grain radius and snow density, a limitation most pronounced at low-frequency channels (Figs.7 and 8). None of the 6 - 36 GHz channels can effectively retrieve snow depth for fresh snow with very fine grains (radius = 0.1 mm). In contrast, the 89 GHz channel can retrieve snow depth across all grain radius states, although it exhibits a clear saturation when snow depth approaches 0.6 m. Moreover, this saturation threshold decreases as the grain radius increases. For coarse snow grains (radius = 0.5 mm), the retrievable range of snow depth shrinks to 0.3 m at 89 GHz.

We evaluated the retrievable range of snow depth from GR(18/6) and GR(36/18) to assess their applicability. GR(36/18) is better suited for fine-grained snow, whereas GR(18/6) exhibits a broader retrievable range for coarse-grained snowpacks that have undergone substantial metamorphism (Fig. 7). Building on this, we evaluated additional GR configurations and found that pairing 36 GHz with lower frequencies (6 or 10 GHz) can extend the effective retrievable range from 0.5 m to 0.6 m (Fig. 8). For GR(18/6), replacing 18 GHz with 23 GHz provides a significant improvement, expanding the applicable grain radius domain from 0.4 - 0.5 mm down to 0.3 - 0.5 mm while maintaining effective retrievability for snow depths up to approximately 1 m. These results underscore a key limitation of GR-based algorithms: incorporating density alone does not resolve microstructural ambiguity, and neglecting grain radius can consequently introduce substantial biases into snow depth estimates.

For GR-based algorithms, sea ice type critically influences snow depth retrievability (Fig. 9). As MYIF increases, the retrievable range of snow depth shrinks, and this degradation is more severe for fine-grained snow. Despite this general loss of information, GR(36/6) may be advantageous. Even for snow over pure MYI, it can still retrieve snow depths up to 0.4 m for moderate grains (radius = 0.3 mm). In contrast, GR algorithms utilizing 18 GHz or 23 GHz TBs are highly vulnerable over MYI surfaces, providing little to no effective snow depth retrievability for snow with grain radius below 0.5 mm. This highlights the necessity of employing either explicit ice type constraints or channel strategies less susceptible to MYI interference.

To conclude, our results provide practical guidance for passive microwave-based snow depth retrieval. A fusion of complementary GR algorithms could improve snow depth retrievals across different snow and sea ice regimes. Ancillary information such as sea ice type, snowfall, and wind speed could be incorporated to prescribe snow and ice conditions (e.g. snow microstructure and layering configuration). This information could facilitate conditional strategies for fusing GRs, consequently enhancing snow depth retrievals. In addition, multi-parameter integrated retrieval (e.g. Scarlat et al., 2017), which simultaneously optimizes snow depth along with other snow-ice physical parameters, provides a physically consistent method for parameter estimation. By explicitly representing coupled parameters, integrated retrieval can suppress error propagation from mis-specified density and microstructure into snow depth, thereby improving transferability across seasonal transitions and mixed ice type conditions.

Code and data availability

The MOSAiC snow measurements used in this study can be found in: https://doi.pangaea.de/10.1594/PANGAEA.935934,
https://doi.pangaea.de/10.1594/PANGAEA.952794 (for snow density and snow grain radius),
https://doi.pangaea.de/10.1594/PANGAEA.940200 (for snow temperature),
https://doi.pangaea.de/10.1594/PANGAEA.946807 (for snow salinity).
The MOSAiC ice core measurements used in this study can be found in https://doi.pangaea.de/10.1594/PANGAEA.971385 and https://doi.pangaea.de/10.1594/PANGAEA.974764.
Both the SMRT model and the EFAST implementation used in this study are open-source Python libraries. The source code of the SMRT model is available at https://github.com/smrt-model/smrt, and the EFAST implementation is available at https://github.com/SALib/SALib.

Author contributions

Ziyu Yan: Conceptualization, Methodology, Software, Writing – original draft. Yufang Ye: Methodology, Writing – review & editing, Supervision, Funding acquisition. Georg Heygster: Methodology, Writing – review & editing, Supervision. Bin Cheng: Visualization, Writing – review & editing, Supervision. Carolina Gabarró: Writing – review & editing. Ferran

Hernández-Macià: Writing – review & editing. Xiao Cheng: Funding acquisition. All authors participated in the interpretation of the results and draft.

Competing interests

At least one of the (co-)authors is a member of the editorial board of The Cryosphere, and the authors have no other competing interests to declare.

Acknowledgements

We sincerely thank the MOSAiC expedition teams and all data providers for their tremendous efforts in collecting, processing, and making the MOSAiC data openly available. We also acknowledge the developers of SMRT for making the model publicly available. Portions of the base imagery in Fig. 1 were generated using OpenAI's image-generation tool and were subsequently edited and formatted by the authors.

Financial support

Ziyu Yan, Yufang Ye and Xiao Cheng were funded through the National Natural Science Foundation of China (Grant No. 42576270), and the Natural Science Foundation of Guangdong Province, China (Grant No. 2026A1515012280) and the Innovation Group Project of Southern Marine Science and Engineering Guangdong Laboratory (Zhuhai) (Grant No. 311021008). Bin Cheng was funded through the Research Council of Finland project IceScales (Grant no. 364939).

References

Arndt, S., Haas, C., Meyer, H., Peeken, I., and Krumpen, T.: Recent observations of superimposed ice and snow ice on sea ice in the northwestern Weddell Sea, The Cryosphere, 15, 4165–4178, 2021, https://doi.org/10.5194/tc-15-4165-2021.

Burgard, C., Notz, D., Pedersen, L., and Tonboe, R.: 25/03/2026, The Cryosphere, 14, 2020, https://doi.org/10.5194/tc-14-2369-2020.

Cox, G. F. and Weeks, W. F.: Equations for determining the gas and brine volumes in sea-ice samples, Journal of Glaciology, 29, 306–316, 1983, https://doi.org/10.3189/S0022143000008364.

Colbeck, S. C.: The capillary effects on water percolation in homogeneous snow, Journal of Glaciology, 13, 85–97, 1974, https://doi.org/10.3189/S002214300002339X.

Cox, G. F. and Weeks, W. F.: Salinity variations in sea ice, Journal of Glaciology, 13, 109–120, 1974, https://doi.org/10.3189/S0022143000023418.

Colbeck, S. C.: An overview of seasonal snow metamorphism, Reviews of Geophysics, 20, 45–61, 1982, https://doi.org/10.1029/RG020i001p00045.

Domine, F., Taillandier, A. S., and Simpson, W. R.: A parameterization of the specific surface area of seasonal snow for field use and for models of snowpack evolution, Journal of Geophysical Research: Earth Surface, 112, F2, 2007, https://doi.org/10.1029/2006JF000512.

Domine, F., Albert, M., Huthwelker, T., Jacobi, H. W., Kokhanovsky, A. A., Lehning, M., Picard G., and Simpson, W. R.: Snow physics as relevant to snow photochemistry, Atmospheric Chemistry and Physics, 8, 171–208, 2008, https://doi.org/10.5194/acp-8-171-2008.

Domine, F.: Physical properties of snow, in: Encyclopedia of Snow, Ice and Glaciers, Springer, Dordrecht, 859–863, 2011.

Frickenhaus, S., Ransby, D., Shupe, M., Jaiser, R., and Nicolaus, M.: Data from the MOSAiC Arctic Ocean drift experiment, Scientific Data, 9, 568, 2022, https://doi.org/10.1038/s41597-022-01678-8.

Fuhrhop, R., Grenfell, T. C., Heygster, G., Johnsen, K. P., Schlüssel, P., Schrader, M., and Simmer, C.: A combined radiative transfer model for sea ice, open ocean, and atmosphere, Radio Science, 33, 303–316, 1998, https://doi.org/10.1029/97RS03020.

Gao, S., Li, Z., Zhang, P., Chen, Q., Huang, L., Zhou, J., Zhao C., Qiao H. and Zheng, Z.: A novel global snow depth retrieval method considering snow metamorphism and forest influence, Remote Sensing of Environment, 295, 113712, 2023, https://doi.org/10.1016/j.rse.2023.113712.

Granskog, M. A., Vihma, T., Pirazzini, R., and Cheng, B.: Superimposed ice formation and surface energy fluxes on sea ice during the spring melt–freeze period in the Baltic Sea, Journal of Glaciology, 52, 119–127, 2006, https://doi.org/10.3189/172756506781828971.

He, L., Xue, B., Hui, F., Xu, S., Chen, Z., and Cheng, X.: Toward daily snow depth estimation on Arctic sea ice during the whole winter season from passive microwave radiometer data, IEEE Transactions on Geoscience and Remote Sensing, 62, 1–15, 2024, https://doi.org/10.1109/TGRS.2024.3358340.

Hou, W., Li, Z., Wang, J., Xu, X., Goloub, P., and Qie, L.: Improving remote sensing of aerosol microphysical properties by near-infrared polarimetric measurements over vegetated land: Information content analysis, Journal of Geophysical Research: Atmospheres, 123, 2215–2243, 2018, https://doi.org/10.1002/2017JD027388.

Kacimi, S. and Kwok, R.: Arctic snow depth, ice thickness, and volume from ICESat-2 and CryoSat-2: 2018–2021, Geophysical Research Letters, 49, e2021GL097448, 2022, https://doi.org/10.1029/2021GL097448.

Kang, D. H., Tan, S., and Kim, E. J.: Evaluation of brightness temperature sensitivity to snowpack physical properties using coupled snow physics and microwave radiative transfer models, IEEE Transactions on Geoscience and Remote Sensing, 57, 10241–10251, 2019, https://doi.org/10.1109/TGRS.2019.2932732.

Leppäranta, M. and Manninen, T.: The brine and gas content of sea ice with attention to low salinities and high temperatures, Finnish Institute of Marine Research, Helsinki, Finland, Internal Report 1988-2, 15, 1988.

Löwe, H. and Picard, G.: Microwave scattering coefficient of snow in MEMLS and DMRT-ML revisited: The relevance of sticky hard spheres and tomography-based estimates of stickiness, The Cryosphere, 9, 2101–2117, 2015, https://doi.org/10.5194/tc-9-2101-2015.

Landrum, L. L. and Holland, M. M.: Influences of changing sea ice and snow thicknesses on simulated Arctic winter heat fluxes, The Cryosphere, 16, 1483–1495, 2022, https://doi.org/10.5194/tc-16-1483-2022.

Macfarlane, A. R., Löwe, H., Gimenes, L., Wagner, D. N., Dadic, R., Ottersberg, R., Hämmerle S., and Schneebeli, M.: Temporospatial variability of snow's thermal conductivity on Arctic sea ice, The Cryosphere, 17, 5417–5434, 2023, https://doi.org/10.5194/tc-17-5417-2023.

Macfarlane, Amy R., Schneebeli, Martin, Dadic, Ruzica, Wagner, David N., Arndt, Stefanie, Clemens-Sewall, David, Hämmerle, Stefan, Hannula, Henna-Reetta, Jaggi, Matthias, Kolabutin, Nikolai, Krampe, Daniela, Lehning, Michael, Matero, Ilkka, Nicolaus, Marcel, Oggier, Marc, Pirazzini, Roberta, Polashenski, Chris, Raphael, Ian, Regnery, Julia, Shimanchuck, Egor, Smith, Madison M., and Tavri, Aikaterini: Snowpit raw data collected during the MOSAiC expedition, PANGAEA [data set], https://doi.org/10.1594/PANGAEA.935934, 2021.

Maksym, T. and Jeffries, M. O.: Phase and compositional evolution of the flooded layer during snow-ice formation on Antarctic sea ice, Annals of Glaciology, 33, 37–44, 2001, https://doi.org/10.3189/172756401781818860.

Markus, T. and Cavalieri, D. J.: Snow depth distribution over sea ice in the Southern Ocean from satellite passive microwave data, in: Antarctic Sea Ice: Physical Processes, Interactions and Variability, 74, 19–39, 1998, https://doi.org/10.1029/AR074p0019.

Marino, S., Hogue, I. B., Ray, C. J., and Kirschner, D. E.: A methodology for performing global uncertainty and sensitivity analysis in systems biology, Journal of Theoretical Biology, 254, 178–196, 2008, https://doi.org/10.1016/j.jtbi.2008.04.011.

Mätzler, C.: Improved Born approximation for scattering of radiation in a granular medium, Journal of Applied Physics, 83, 6111–6117, 1998, https://doi.org/10.1063/1.367496.

Merkouriadi, I., Liston, G. E., Graham, R. M., and Granskog, M. A.: Quantifying the potential for snow-ice formation in the Arctic Ocean, Geophysical Research Letters, 47, 2020, https://doi.org/10.1029/2019GL085020.

Merkouriadi, I., Cheng, B., Graham, R. M., Rösel, A., and Granskog, M. A.: Critical role of snow on sea ice growth in the Atlantic sector of the Arctic Ocean, Geophysical Research Letters, 44, 10–479, 2017, https://doi.org/10.1002/2017GL075494.

Notz, D. and Worster, M. G.: Desalination processes of sea ice revisited, Journal of Geophysical Research: Oceans, 114, C5, 2009, https://doi.org/10.1029/2008JC004885.

Nicolaus, M., Perovich, D. K., Spreen, G., Granskog, M. A., von Albedyll, L., Angelopoulos, M., Anhaus, P., Arndt, S., Jakob Belter, H., Bessonov, V., Birnbaum, G., Brauchle, J., Calmer, R., Cardellach, E., Cheng, B., Clemens-Sewall, D., Dadic, R., Damm, E., de Boer, G., Demir, O., Dethloff, K., Divine, D. V., Fong, A. A., Fons, S., Frey, M. M., Fuchs, N., Gabarró, C., Gerland, S., Goessling, H. F., Gradinger, R., Haapala, J., Haas, C., Hamilton, J., Hannula, H. R., Hendricks, S., Herber, A., Heuzé, C., Hoppmann, M., Høyland, K. V., Huntemann, M., Hutchings, J. K., Hwang, B., Itkin, P., Jacobi, H. W., Jaggi, M., Jutila, A., Kaleschke, L., Katlein, C., Kolabutin, N., Krampe, D., Kristensen, S. S., Krumpen, T., Kurtz, N., Lampert, A., Lange, B. A., Lei, R., Light, B., Linhardt, F., Liston, G. E., Loose, B., Macfarlane, A. R., Mahmud, M., Matero, I. O., Maus, S., Morgenstern, A., Naderpour, R., Nandan, V., Niubom, A., Oggier, M., Oppelt, N., Pätzold, F., Perron, C., Petrovsky, T., Pirazzini, R., Polashenski, C., Rabe, B., Raphael, I. A., Regnery, J., Rex, M., Ricker, R., Riemann-Campe, K., Rinke, A., Rohde, J., Salganik, E., Scharien, R. K., Schiller, M., Schneebeli, M., Semmling, M., Shimanshuck, E., Shupe, M. D., Smith, M. M., Smolyanitsky, V., Sokolov, V., Stanton, T. P., Stroeve, J., Thielke, L., Timofeeva, A., Tonboe, R. T., Tavri, A., Tsamados, M., Wagner, D. N., Watkins, D., Webster, M., and Wendisch, M.: Overview of the MOSAiC expedition: Snow and sea ice, Elem. Sci. Anth., 10, 000046, 2022, https://doi.org/10.1525/elementa.2021.000046.

Nicolaus, M., Haas, C., and Bareiss, J.: Observations of superimposed ice formation at melt-onset on fast ice on Kongsfjorden, Svalbard, Physics and Chemistry of the Earth, Parts A/B/C, 28, 1241–1248, 2003, https://doi.org/10.1016/j.pce.2003.08.048.

Ottaviani, M., Myers, G. H., and Chen, N.: Global sensitivity analysis of simulated remote sensing polarimetric observations over snow, Atmospheric Measurement Techniques, 17, 4737–4756, 2024, https://doi.org/10.5194/amt-17-4737-2024.

Oggier, Marc, Salganik, Evgenii, Whitmore, Laura M., Fong, Allison A., Hoppe, Clara Jule Marie, Rember, Robert, Høyland, Knut Vilhelm, Gradinger, Rolf, Divine, Dmitry V., Fons, Steven W., Abrahamsson, Katarina, Aguilar-Islas, Ana M., Angelopoulos, Michael, Arndt, Stefanie, Balmonte, John Paul, Bozzato, Deborah, Bowman, Jeff S., Castellani, Giulia, Chamberlain, Emelia, Creamean, Jessie, D'Angelo, Alessandra, Damm, Ellen, Dietrich, Ulrike, Droste, Elise Sayana, Dumitrascu, Adela, Eggers, Lena, Gardner, Jessie, Grosfeld, Lisa, Haapala, Jari, Heitmann, Laura, Immerz, Antonia, Kolabutin, Nikolai, Lange, Benjamin Allen, Lei, Ruibo, Marsay, Christopher M., Maus, Sönke, Müller, Oliver, Olsen, Lasse Mørk, Nuibom, Alexey, Ren, Jian, Rinke, Annette, Schmidt, Katrin, Sheikin, Igor, Shimanchuk, Egor, Snoeijs-Leijonmalm, Pauline, Spahic, Susanne, Stefels, Jacqueline, Torres-Valdés, Sinhué, Torstensson, Anders, Ulfsbo, Adam, Verdugo, Josefa, Vortkamp, Martina, Wang, Lei, Webster, Melinda, and Granskog, Mats A.: First-year sea-ice salinity, temperature, density, nutrient, oxygen and hydrogen isotope composition from the main coring site (MCS-FYI) during MOSAiC legs 1 to 4 in 2019/2020, version 2, PANGAEA [data set], https://doi.org/10.1594/PANGAEA.971385, 2024.

Oggier, Marc, Salganik, Evgenii, Whitmore, Laura M., Fong, Allison A., Hoppe, Clara Jule Marie, Rember, Robert, Høyland, Knut Vilhelm, Gradinger, Rolf, Divine, Dmitry V., Fons, Steven W., Abrahamsson, Katarina, Aguilar-Islas, Ana M., Angelopoulos, Michael, Arndt, Stefanie, Balmonte, John Paul, Bozzato, Deborah, Bowman, Jeff S., Castellani, Giulia, Chamberlain, Emelia, Creamean, Jessie, D'Angelo, Alessandra, Damm, Ellen, Dietrich, Ulrike, Droste, Elise Sayana, Dumitrascu, Adela, Eggers, Sarah Lena, Gardner, Jessie, Grosfeld, Lisa, Haapala, Jari, Heitmann, Laura, Immerz, Antonia, Kolabutin, Nikolai, Lange, Benjamin Allen, Lei, Ruibo, Marsay, Christopher M., Maus, Sönke, Olsen, Lasse Mørk, Müller, Oliver, Nuibom, Alexey, Ren, Jian, Rinke, Annette, Schmidt, Katrin, Sheikin, Igor, Shimanchuk, Egor, Snoeijs-Leijonmalm, Pauline, Spahic, Susanne, Stefels, Jacqueline, Torres-Valdés, Sinhué, Torstensson, Anders, Ulfsbo, Adam, Verdugo, Josefa, Vortkamp, Martina, Wang, Lei, Webster, Melinda, and Granskog, Mats A.: Second-year sea-ice salinity, temperature, density, nutrient, oxygen and hydrogen isotope composition from the main coring site (MCS-SYI) during MOSAiC legs 1 to 4 in 2019/2020, version 2, PANGAEA [data set], https://doi.org/10.1594/PANGAEA.974764, 2025.

Picard, G., Brucker, L., Roy, A., Dupont, F., Fily, M., Royer, A., and Harlow, C.: Simulation of the microwave emission of multi-layered snowpacks using the dense media radiative transfer theory: The DMRT-ML model, Geoscientific Model Development, 6, 1061–1078, 2013, https://doi.org/10.5194/gmd-6-1061-2013.

Picard, G., Sandells, M., and Löwe, H.: SMRT: An active–passive microwave radiative transfer model for snow with multiple microstructure and scattering formulations (v1.0), Geoscientific Model Development, 11, 2763–2788, 2018, https://doi.org/10.5194/gmd-11-2763-2018.

Picard, G., Löwe, H., Domine, F., Arnaud, L., Larue, F., Favier, V., Le Meur, E., Lefebvre, E., Savarino, J., and Royer, A.: The microwave snow grain size: A new concept to predict satellite observations over snow-covered regions, AGU Advances, 3, e2021AV000630, 2022a, https://doi.org/10.1029/2021AV000630.

Picard, G., Leduc-Leballeur, M., Banwell, A. F., Brucker, L., and Macelloni, G.: The sensitivity of satellite microwave observations to liquid water in the Antarctic snowpack, The Cryosphere, 16, 5061–5083, 2022b, https://doi.org/10.5194/tc-16-5061-2022.

Rostosky, P., Spreen, G., Farrell, S. L., Frost, T., Heygster, G., and Melsheimer, C.: Snow depth retrieval on Arctic sea ice from passive microwave radiometers—Improvements and extensions to multiyear ice using lower frequencies, Journal of Geophysical Research: Oceans, 123, 7120–7138, 2018, https://doi.org/10.1029/2018JC014028.

Rodgers, C. D.: Inverse Methods for Atmospheric Sounding: Theory and Practice, World Scientific Publishing Co. Pte. Ltd., London, 2000.

Rückert, J. E., Huntemann, M., Tonboe, R. T., and Spreen, G.: Modeling snow and ice microwave emissions in the Arctic for a multi-parameter retrieval of surface and atmospheric variables from microwave radiometer satellite data, Earth and Space Science, 10, e2023EA003177, 2023, https://doi.org/10.1029/2023EA003177.

Saltelli, A., Tarantola, S., and Chan, K. S.: A quantitative model-independent method for global sensitivity analysis of model output, Technometrics, 41, 39–56, 1999, https://doi.org/10.1080/00401706.1999.10485594.

Scarlat, R. C., Heygster, G., and Pedersen, L. T.: Experiences with an optimal estimation algorithm for surface and atmospheric parameter retrieval from passive microwave data in the Arctic, IEEE Journal of Selected Topics in Applied Earth Observations and Remote Sensing, 10, 3934–3947, 2017, https://doi.org/10.1109/JSTARS.2017.2739858.

https://doi.org/10.5194/egusphere-2026-1680
Preprint. Discussion started: 28 May 2026

Shokr, M. E. and Sinha, N. K.: Arctic sea ice microstructure observations relevant to microwave scattering, Arctic, 265–279, 1994, http://www.jstor.org/stable/40511575.

Sturm, M. and Benson, C. S.: Vapor transport, grain growth and depth-hoar development in the subarctic snow, Journal of Glaciology, 43, 42–59, 1997, https://doi.org/10.3189/S0022143000002793.

Sturm, M., Holmgren, J., and Perovich, D. K.: Winter snow cover on the sea ice of the Arctic Ocean at the Surface Heat Budget of the Arctic Ocean (SHEBA): Temporal evolution and spatial variability, Journal of Geophysical Research: Oceans, 107, SHE-23, 2002, https://doi.org/10.1029/2000JC000400.

Soriot, C., Picard, G., Prigent, C., Frappart, F., and Domine, F.: Year-round sea ice and snow characterization from combined passive and active microwave observations and radiative transfer modeling, Remote Sensing of Environment, 278, 113061, 2022, https://doi.org/10.1016/j.rse.2022.113061.

Schleef, S., Löwe, H., and Schneebeli, M.: Influence of stress, temperature and crystal morphology on isothermal densification and specific surface area decrease of new snow, The Cryosphere, 8, 1825–1838, 2014, https://doi.org/10.5194/tc-8-1825-2014.

Stöffelmair, U., Popp, T., Vountas, M., and Bösch, H.: Aerosol composition retrieval from a combination of three different spaceborne instruments: information content analysis, Atmos. Meas. Tech., 18, 2005–2020, https://doi.org/10.5194/amt-18-2005-2025, 2025.

Tarantola, A.: Inverse problem theory and methods for model parameter estimation, Society for Industrial and Applied Mathematics, 2005.

Tonboe, R. T.: The simulated sea ice thermal microwave emission at window and sounding frequencies, Tellus A: Dynamic Meteorology and Oceanography, 62, 333–344, 2010, doi: 10.1111/j.1600-0870.2009.00434.x.

Vérin, G., Domine, F., Babin, M., Picard, G., and Arnaud, L.: Metamorphism of snow on Arctic sea ice during the melt season: Impact on spectral albedo and radiative fluxes through snow, The Cryosphere, 16, 3431–3449, 2022, https://doi.org/10.5194/tc-16-3431-2022.

Vargel, C., Royer, A., St-Jean-Rondeau, O., Picard, G., Roy, A., Sasseville, V., and Langlois, A.: Arctic and subarctic snow microstructure analysis for microwave brightness temperature simulations, Remote Sensing of Environment, 242, 111754, 2020, https://doi.org/10.1016/j.rse.2020.111754.

Vuyovich, C. M., Jacobs, J. M., Hiemstra, C. A., and Deeb, E. J.: Effect of spatial variability of wet snow on modeled and observed microwave emissions, Remote Sensing of Environment, 198, 310–320, 2017, https://doi.org/10.1016/j.rse.2017.06.016.

Welch, J. J. and Kelly, R. E.: A prototype passive microwave retrieval algorithm for tundra snow density, The Cryosphere, 19, 5259–5282, 2025, https://doi.org/10.5194/tc-19-5259-2025.

Wivell, K., Fox, S., Sandells, M., Harlow, C., Essery, R., and Rutter, N.: Evaluating Snow Microwave Radiative Transfer (SMRT) model emissivities with 89 to 243 GHz observations of Arctic tundra snow, The Cryosphere, 17, 4325–4341, 2023, https://doi.org/10.5194/tc-17-4325-2023.

Wever, N., Fierz, C., Mitterer, C., Hirashima, H., and Lehning, M.: Solving Richards equation for snow improves snowpack meltwater runoff estimations in detailed multi-layer snowpack model, The Cryosphere, 8, 257–274, 2014, https://doi.org/10.5194/tc-8-257-2014.

Wever, N., Würzer, S., Fierz, C., and Lehning, M.: Simulating ice layer formation under the presence of preferential flow in layered snowpacks, The Cryosphere, 10, 2731–2744, 2016, https://doi.org/10.5194/tc-10-2731-2016.

Yang, J. W., Jiang, L. M., Lemmetyinen, J., Pan, J. M., Luojus, K., and Takala, M.: Improving snow depth estimation by coupling HUT-optimized effective snow grain size parameters with the random forest approach, Remote Sensing of Environment, 264, 112630, 2021, https://doi.org/10.1016/j.rse.2021.112630.

Ye, Y., Yan, Z., Wang, X., Chen, Z., Shokr, M., and Cheng, X.: Influence of radiative transfer model-based atmospheric correction and dynamic tie points on sea ice concentration retrieval from near-90 GHz algorithm with FY-3D MWRI data, IEEE Transactions on Geoscience and Remote Sensing, 2025, https://doi.org/10.1109/TGRS.2025.3551941.

Zhou, L., Stroeve, J., Xu, S., Petty, A., Tilling, R., Winstrup, M., Rostosky, P., Lawrence, R., Liston, E., Ridout, A., Tsamados, M. and Nandan, V.: Inter-comparison of snow depth over Arctic sea ice from reanalysis reconstructions and satellite retrieval, The Cryosphere, 15, 345–367, 2021, https://doi.org/10.5194/tc-15-345-2021.